Article

Analysis of Vertical Wind Shear Effects on Offshore Wind Energy Prediction Accuracy Applying Rotor Equivalent Wind Speed and the Relationship with Atmospheric Stability

Geon Hwa Ryu [1] , **Dongjin Kim** [2] , **Dae-Young Kim** [3], **Young-Gon Kim** [4], **Sung Jo Kwak** [5], **Man Soo Choi** [6], **Wonbae Jeon** [7] , **Bum-Suk Kim** [3] **and Chae-Joo Moon** [8,*]

[1] Interdisciplinary Program of Renewable Energy Engineering, Mokpo National University, Mokpo 58554, Korea; geonhwa@eiuca.or.kr
[2] Division of Earth Environmental System, Pusan National University, Busan 46241, Korea; ehdwls146@pusan.ac.kr
[3] Faculty of Wind Energy Engineering Graduate School, Jeju National University, Jeju 64243, Korea; kimdy@jejunu.ac.kr (D.-Y.K.); bkim@jejunu.ac.kr (B.-S.K.)
[4] Wind Energy Research Center, Energy Valley Industry-University Convergence Agency, Naju 58277, Korea; ygkim@eiuca.or.kr
[5] Wind Energy Research Team, Korea Institute of Energy Research, Jeju 63357, Korea; sungjo@kier.re.kr
[6] Wind & Marine Energy Department, Green Energy Institute, Mokpo 58656, Korea; mschoi@gei.re.kr
[7] Department of Atmospheric Sciences, Pusan National University, Busan 46241, Korea; wbjeon@pusan.ac.kr
[8] Department of Electrical and Control Engineering, Mokpo National University, Mokpo 58554, Korea
* Correspondence: cjmoon@mokpo.ac.kr

Abstract: If the wind speed that passed through a wind turbine rotor disk area is constant, the hub height wind speed (HHWS) could be representative of the wind speed over the rotor disk area. However, this assumption cannot be applied to the large wind turbine, because of the wind shear effect by atmospheric stability. This is because the hub height wind speed cannot represent the vertical wind shear effect from the aerodynamics characteristic on the wind turbine. Using SCADA and offshore LiDAR observation data of the Anholt offshore wind farm, it is investigated whether the rotor equivalent wind speed (REWS) introduced in IEC61400-12-1 can contribute to the improvement of power output forecasting accuracy. The weighted value by separated sector area and vertical wind shear effect by difference between heights can explain the role of energy flux and atmospheric stability on the exact wind energy calculation. The commercial CFD model WindSim is used to calculate power production according to the HHWS and the REWS, and to compare them with the actual AEP of the local wind farm. The classification of atmospheric stability is carried out by Richardson number, which well represents the thermal and physical properties of the atmosphere below the atmospheric boundary layer, along with the wind shear coefficient and turbulence intensity. When atmospheric stability was classified by each stability index, the REWS-based predicted power output was sometimes more accurate than HHWS, but sometimes inferior. However, in most cases, using the REWS, it was possible to calculate an estimate closer to the actual power output. Through the results of this study, it is possible to provide a rationale for which method, REWS or HHWS, can more accurately calculate the expected power output and effectively derive the economic feasibility of the project by identifying the characteristics of local atmospheric stability before the wind farm project.

Keywords: rotor equivalent wind speed; hub height wind speed; wind shear; atmospheric stability; offshore wind energy; Richardson number

1. Introduction

Climate change has become the greatest threat to humanity and nature in this century, and this is being driven by the increase in greenhouse gas emissions, especially from the energy sector, which accounts for more than 60% of the global total [1,2]. Therefore,

energy systems worldwide have inevitably undergone radical changes with the transition to sustainable, renewable, and clean energy sources [3,4]. Meanwhile, following the Paris Agreement, in November 2021 the 26th Conference of the Parties (COP26) adopted the Glasgow Climate Pact, and the declaration was made on gas reduction and investments for decarbonization [5]. The financial institutions of governments participating in COP26 agreed to stop public support for the fossil fuel energy sector and, in the future, to increase support for clean renewable energy conversion. South Korea is also participating in the gradual abolition of coal power plants, and the cessation of new construction and investment [6–8].

This decarbonization trend in South Korea is led by the 3rd Basic Energy Plan, the Renewable Energy 3020 Implementation Plan to increase the proportion of renewable energy to 20% by 2030, and the Korean Green New Deal, which aims to achieve a green transition by establishing a carbon-neutral promotion base and the realization of carbon neutrality with the goal of 2050 [9,10]. Among the various means for building a decarbonized society and responding to climate change, the energy transition to renewable energy is recognized as the most important method, because it is converging to grid parity as price competitiveness is continuously improved, compared to fossil fuels. Among them, wind energy is promoting the step-by-step process of measuring wind resources and supporting feasibility studies in up to 13 regions for the site selection of large-scale offshore wind farms. Through this plan, a total of 17.7 GW wind farm facilities will be built by 2030 [11–13].

Meanwhile, domestic and foreign wind turbine manufacturers have developed generators with unit capacity of more than 10 MW and obtained type certification since 2018 [14,15]. Vestas V236-15MW, GE Haliade-X 14.0, Siemens-Gamesa SG14-222DD, and Mingyang MySE 16.0-242 wind turbines have already been certified for prototype production and commercialization. All these super-large offshore wind turbines have a rotor diameter that exceeds 220 m. In a similar fashion, global wind turbine manufacturers are continuously developing products in the direction of expanding the capacity of the single turbine [16,17]. This is because in constructing a wind farm, it is more economic and more advantageous to install a small number of wind turbines, each with a large capacity, than to install many wind turbines, each with a small capacity. According to Rystad Energy Research and Analysis, if a 14 MW class turbine is used instead of a 10 MW wind turbine to construct a 1 GW wind farm, it will cost about USD 100 million in turbine manufacturing cost, foundation substructure manufacturing cost, installation cost, and cable array cost, and savings can be obtained [18]. As the wind farm can be scaled up by the cost savings, turbine manufacturers continue to develop larger-capacity turbines.

As the capacity and scale of wind turbines increase, accurate measurement of power curves, and the calculation of expected power generation are required, and conflicting interests arise in that regard [19,20]. Traditionally, to calculate the expected power generation of a wind turbine, only the wind speed at a single height corresponding to the hub height is considered, under the assumption that atmospheric stability is in a near-neutral state [21–23]. This was proper in the past to apply to small wind turbines with short blade lengths, and in calm offshore or flat land without obstacles, the difference in wind speed by height is small. So even if the expected power generation was calculated by selecting the hub height wind speed as the representative wind speed within the rotor disk, the error compared with the actual power generation was not large [21,22]. However, in recent years, as the diameter of the rotor area of the wind turbine has exceeded 200 m, the hub height wind speed cannot be the representative value in complex terrain, such as mountains, or even in flat terrain, where wind speed fluctuations by height occur in short time, due to the meteorological characteristics within the local atmospheric boundary layer. In regions showing these characteristics, to analyze the effect of the difference in wind speed by height on power generation, it is necessary to consider several wind speeds corresponding to multiple heights at the same time [24–26]. Moreover, a detailed cause analysis is required that correlates atmospheric stability with the time when large wind speed difference by height occurs. The International Electrotechnical Commission (IEC) proposes a method to

calculate the rotor equivalent wind speed by using the wind speed measured at (at least) three random heights [27]. It is maintained that the effect of the kinetic energy flux of the wind speed passing through the rotor disk area can be reflected in the power generation calculation considering the vertical wind shear [27].

In foreign countries, the concept has been introduced, and empirical studies of the rotor equivalent wind speed have already been actively conducted. The IEC Technical Committee 88 (TC88) recognizes that if the wind shear coefficient is kept constant, the difference between the rotor equivalent wind speed and the hub height wind speed is generally small [24]. However, in special cases, the vertical wind speed profile cannot be sufficiently explained by a constant wind shear coefficient, and such cases may be influenced by local meteorological characteristics or atmospheric stability distribution [12,21,22]. In this case, it is necessary to recognize that the difference between the rotor equivalent wind speed and the hub height wind speed may be considerable. In particular, it was revealed that the vertical wind speed shear of the rotor disk shows a difference in speed gradient according to atmospheric stability, and that this difference in vertical wind speed causes a change in the average wind speed [28]. In addition, the scattering of the data collected by the output curve of the wind turbine was analyzed less when using the rotor equivalent wind speed [23,29]. It was recommended to use the rotor equivalent wind speed in the area outside the wind shear coefficient of (-0.05–0.4) [24], and claimed that REWS helps to improve the accuracy in the area where non-linear strong wind shear occurs [30]. As a result of predicting wind power generation output according to physical patterns by correlating meteorological characteristics and rotor equivalent wind speed through machine learning, it was confirmed that the prediction accuracy was improved by 22% [31]. In addition, since both the vertical wind shear and the horizontal wind shear (wind direction shear) can affect the amount of power generation, a new formula applied to the rotor equivalent wind speed has also been proposed [32–34]. In addition, the wind power generation based on the rotor equivalent wind speed can quantify the sensitivity to wind speed shear and direction change, as well as atmospheric stability [35–37].

On the other hand, it has been revealed that there is a statistically significant difference between the applied output curve and the conventional output curve in a form that considers atmospheric stability variables, such as the strength of wind turbulence passing through the rotor disk, the Richardson number, and the Monin–Obukhov length [12,38–41]. Since such atmospheric stability can have a significant effect on both the amount of power generation of a wind turbine, and stability and durability, a thorough preliminary investigation is absolutely required [12].

The purpose of this study is to determine the potential accuracy and value of the rotor equivalent wind speed recommended by IEC 61400-12-1. The purpose of this study is to investigate whether REWS, which is theoretically better and suitable for very large wind turbines, can always produce better prediction results in the Danish offshore environment. To this end, the simulated power output using HHWS and REWS are simulated by analyzing SCADA data and offshore LiDAR data of the Anholt offshore wind farm in actual operation. This predicted values were verified by comparing it with the actual power output of the offshore wind farm for two years, and if the error rate was significantly improved or not improved, the cause was analyzed through correlation with the atmospheric stability distribution. Wind shear coefficient, turbulence intensity, and Richardson number were used as atmospheric stability indicators, which are universal criteria for judging mechanical or thermal atmospheric stability.

2. Materials and Methods

2.1. The Anholt Offshore Wind Farm

The wind farm site to be studied is the Anholt offshore wind farm in Denmark operated by Ørsted, the world's largest offshore wind farm developer. The Anholt Offshore Wind Farm is located between Djursland and Anholt island in the Kattegat Sea of Denmark, and has a capacity of 400 megawatts. The Anholt offshore wind farm was the largest offshore

wind farm in Denmark until 2019, before the completion of the Horns Rev Phase 3 offshore wind farm. It has a large-scale project area that is equivalent to four times the area of Anholt island (long axis length of 20 km, average width 5 km, total area 88 km^2), and 111 Siemens SWT 3.6-120 model wind turbines are installed [42,43].

The substructure type is in the form of a monopile, and the water depth of the project sea area is approximately (15–19) m, which is not deep, and is about 15 km distance from the shoreline. The wind farm was completed in the summer of 2013, and is large enough to support the annual electricity consumption of 400,000 Danish households (4% of the total electricity consumption of Denmark). Figure 1 shows the site location and photography of the Anholt offshore wind farm, while Table 1 provides technical information of the wind farm and SCADA data. It was determined that a very large amount of data were required to analyze the power generation of all wind turbines, and the main wind shear effect could not be properly reflected, due to the overlapping wake effect. As will be introduced later, only five wind turbines (A1, A2, A3, B1, and C1) enlarged in orange color were selected and analyzed, considering that the main wind direction observed from LiDAR was southwest. This is to, as much as possible, use only the wind turbine located on the upwind side, to minimize the wake effect applied to the rotor equivalent wind speed analysis.

Figure 1. Left: Location of the Anholt offshore wind farm. Right: Arrangement of 111 offshore wind turbines. The offshore LiDAR is marked as dark-blue square to the west of Anholt wind farm. Only the five identified wind turbines (A1–A3, B1, and C1) marked in orange color in the enlarged figure are used for this analysis.

Table 1. Key information of the Anholt offshore wind farm, wind turbines, and SCADA data information in Denmark.

Item		Content
Offshore wind farm	Wind turbines	Siemens Gamesa Renewable Energy, SWT 3.6-120
	Number of wind turbines	111
	Wind turbine capacity [MW]	3.6
	Total capacity [MW]	400
	Hub height [m]	81.6
	Rotor diameter [m]	120
	Length of monopile [m]	37–55
	Water depth [m]	15–19
	Distance to shore [km]	15 (Based on the nearest wind turbine)
	Offshore wind farm area [km^2]	88
	Commissioned	Summer 2013
SCADA	Data	WTG [1] coordinates, SCADA data with min/max/mean/stddev [2] (Wind speed, Yaw position, Blade pitch position, RPM, Active power, Ambient temperature)

[1] Wind turbine generator, [2] Standard deviation.

2.2. Offshore Wind LiDAR

The Offshore Light Detection and Ranging (LiDAR) is the WindCube model manufactured by Leosphere, and is located to the west of the offshore wind farm. WindCube LiDAR uses pulsed heterodyne technology to rotate and radiate a laser beam with a wavelength of 1.54 μm in a cone shape. After scanning the 4 beamlines radiating at intervals of 90 degrees, the three-dimensional wind direction and wind speed are calculated at 10 heights by geometric calculation. The wind speed vector is calculated by detecting the Doppler shift of the laser due to fine dust following the atmospheric flow from a sampling volume of 20 m configured along the beamline. LiDAR is installed on an offshore platform at a height of 25.6 m from the Lowest Astronomical Tide (LAT), and 10 min averaged observation data for a total of 2 years from 1 January 2013 to 31 December 2014 were used for analysis. In this study, the analysis was performed assuming that the height is simply 25 m. Wind speed and direction were observed at 10 levels from (40 to 290) m, and air pressure, humidity, and temperature were observed at a single height near the sea surface. Table 2 shows the key information of the LiDAR and meteorological observation data.

Table 2. Key information of the LiDAR in the Anholt offshore wind farm.

Item		Content
Type		Leosphere WindCube
Measurement period		2013.01.01–2014.12.31
Height above MSL [1] [m]		25.6
Location		56.595664° N, 11.152728° E
	Wind speed	40, 60, 76, 80, 100, 116, 160, 200, 250, 290
	Wind direction	40, 60, 76, 80, 100, 116, 160, 200, 250, 290
Observation height [m]	Air pressure	2
	Relative humidity	2
	Air temperature	2

[1] To correctly calculate the measuring height above Lowest Astronomical Tide (LAT), the height of the LiDAR lens above LAT ($\approx$25.6 m) must be considered. For example, if the configured measuring height is 10.0 m, the true height where measurement is taken is 35.6 m above the LAT.

2.3. Rotor Equivalent Wind Speed

Traditionally, it has been judged that the wind speed at the hub height, which is the center of the rotor disk area, is the average wind speed of the wind passing through the entire rotor disk under the assumption that atmospheric stability is near-neutral, and the wind speed constantly increases with height. However, when atmospheric stability is near-neutral or weakly stable, or for small and medium-sized wind turbines with a rotor disk diameter of less than 50 m, this is a suitable method. As wind turbines have recently become super-sized, the rotor equivalent wind speed is recommended, which can take into account the effect of changes in kinetic energy on power generation [21,22]. This is a principle that considers wind speed at various heights passing through the rotor disk area by horizontally multiple divisions, as shown in Figure 2.

The rotor equivalent wind speed u_{eq} is defined as shown in Equation (1):

$$u_{eq} = \sqrt[3]{\sum_{i=1}^{n_h} \frac{A_i}{A} u_i^3} \tag{1}$$

where A is the total area of the rotor disk, A_i is the area of the i-th segment of the rotor disk, and u_i is the wind speed at each segment height. That is, A_i/A may represent a partial weighting value with respect to the rotor disk area, and imply the momentum of the entire rotor disk area by multiplying it by the wind speed passing through each sector. A_i can be calculated through Equation (2), which can be easily obtained with the arc cosine function. It is assumed that the radius of the rotor rotation area is R, and the height of the sector is h when setting the first sector from the top (Figure 3). The length of h can be calculated

through Equation (3), where H and D mean the hub height and the rotor disk diameter, respectively. The relative ratio of HHWS and REWS can be found from Equation (4).

$$A_i = R^2 cos^{-1}\left(\frac{R-h}{R}\right) - (R-h)\sqrt{2Rh-h^2} \tag{2}$$

$$h_i = H + \frac{1}{n_h}\left[i - \left(\frac{n_h+1}{2}\right)\right]D \tag{3}$$

$$\frac{V_{REWS}}{V_{HHWS}} = \sqrt[3]{\sum_{i=1}^{n_h}\frac{A_i}{A}\left[1 + \frac{1}{n_h}\left(i - \left(\frac{n_h+1}{2}\right)\right)\frac{D}{H}\right]^{3\alpha}} \tag{4}$$
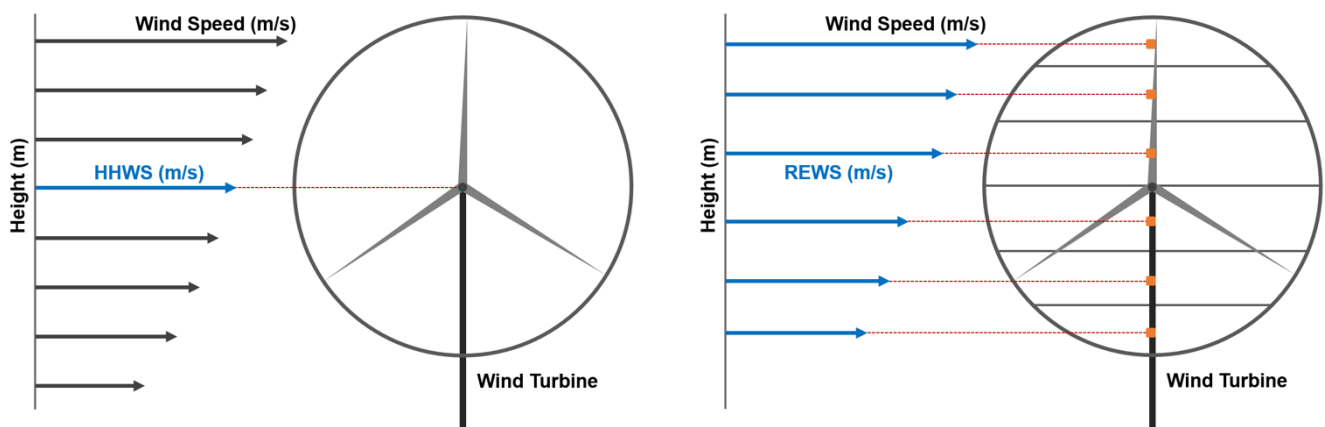

Figure 2. (**Left**) Hub height wind speed (HHWS). The power generation is calculated by considering only the single-height wind speed corresponding to the hub height, which is the center of the rotor disk area. (**Right**) Rotor equivalent wind speed (REWS). The power generation is calculated by dividing the rotor disk area into several horizontal bands, and considering each height wind speed difference passing through the divided area, respectively.
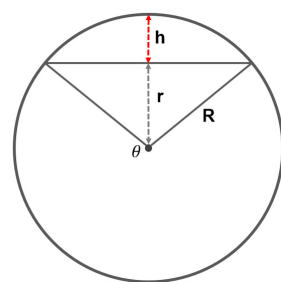

Figure 3. Concept for calculating the equivalent wind speed.

2.4. Atmospheric Stability

Atmospheric stability is an important indicator used to characterize atmospheric turbulence, or to describe the magnitude of atmospheric particle diffusion. In other words, it is the degree to which a slight disturbance of the atmosphere in mechanical equilibrium is likely to return to its original state, or significantly change the atmospheric state. The ratings of atmospheric stability can generally be divided into three levels: unstable, neutral, and stable. Atmospheric stability can be broadly classified into mechanical stability and thermal stability, according to the mediator factors that change atmospheric characteristics. A representative classification method of mechanical atmospheric stability is the vertical wind shear coefficient, which is a principle that determines the degree of fluid flow and diffusion by the transfer of momentum according to the difference in wind speed for each

altitude in the z-direction. Thermal stabilities, such as the Richardson number and Monin–Obukhov length, take into account differences in momentum due to wind speed, as well as thermal motion effects due to temperature and heat flux. Table 3 shows the atmospheric stability classification criteria for each factor and representative meteorological phenomena.

Table 3. Atmospheric stability indices criteria and boundary layer properties.

Stability Class	Wind Shear	TI [1]	Richardson Number	Boundary Layer Properties
Strongly Unstable	$\alpha < 0.0$	$TI \geq 0.15$	$Ri < -0.86$	Lowest Wind Speed/Shear, Highly TI
Unstable	$0.0 \leq \alpha < 0.1$	$0.11 \leq TI < 0.15$	$-0.86 \leq Ri < -0.1$	Lower Wind Speed/Shear, High TI
Near-Neutral	$0.1 \leq \alpha < 0.2$	$0.08 \leq TI < 0.11$	$-0.1 \leq Ri < 0.053$	Logarithmic wind profile
Stable	$0.2 \leq \alpha < 0.3$	$0.05 \leq TI < 0.08$	$0.053 \leq Ri < 0.134$	High Wind Speed/Shear, Nocturnal LLJ [2], Low TI
Strongly Stable	$\alpha \geq 0.3$	$TI < 0.05$	$Ri \geq 0.134$	Highest Wind Speed/Shear, Nocturnal LLJ, Lowest TI

[1] Turbulence intensity, [2] Low-level jet.

In this study, characteristics changes of HHWS and REWS according to local atmospheric stability near offshore wind farms were analyzed through Richardson number, wind shear coefficient, and turbulence analysis. In addition, after calculating the expected energy production using HHWS and REWS, comparative analysis was performed with the actual power generation, and detailed meteorological cause analysis related to atmospheric stability was also performed at the time-point showing significant difference.

2.4.1. Wind Shear Exponent

The power law describes a functional relationship between two numbers that theoretically express the wind speed at one height in exponential form of the wind speed at another height. When the atmospheric stability is close to near-neutral, the vertical wind speed distribution in which the wind speed constantly increases with height appears in the lower atmospheric boundary layer, so that the power law can reasonably be applied. In general, in this case, the vertical wind shear exponent (α) or power law exponent represents a value of 1/7 (≈ 0.143). Based on the approximate value of the vertical wind shear exponent of 0.143, the region showing a high value is a stable atmosphere, and an exponent lower than this means that an unstable atmosphere is dominant. The vertical shear exponent can be obtained through Equation (5):

$$\frac{V}{V_r} = \left(\frac{H}{H_r} \right)^{\alpha} \tag{5}$$

where H [m] is the target height, H_r [m] is the reference height, V [ms^{-1}] is the wind speed at the target height, and V_r [ms^{-1}] is the wind speed at the reference height. Wind shear exponents can be obtained if wind speed measurements for at least two heights are available by fitting wind speed data with Equation (6):

$$\alpha = \frac{\ln(V) - \ln(V_r)}{\ln(H) - \ln(H_r)} \tag{6}$$

2.4.2. Turbulence Intensity (TI)

Meteorological parameters related wind resources can be important influencing factors on wind turbine performance and load. Among them, the turbulence component is a representative parameter, and turbulence measurement is generally performed using equipment, such as cup anemometer, sonic anemometer, and LiDAR. Another detail is

that IEC 61400-12-1 requires measuring the horizontal/vertical component of a wind resource, so that the strength of turbulence can be analyzed with its horizontal/vertical component. Turbulence intensity is a detailed theory constituting the governing equation of turbulence along with the continuity equation and Navier–Stokes equation. When the flow is classified into the average value and the fluctuation value, this indicates the degree of fluctuation compared to the average value. The turbulence intensity can be calculated with Equation (7):

$$\text{TI} = \frac{\sigma V}{V} \tag{7}$$

2.4.3. Richardson Number

The properties and relative magnitudes of turbulence produced by mechanical or thermal convection can be determined by the Richardson number. This is a stability index that can take into account the density difference and wind speed difference in the atmosphere by simultaneously measuring the temperature and wind speed of the upper and lower layers. When defining the Richardson number, it is preferred to first define the stability parameter S (Equation (8)). The variable S is proportional to the rate at which the steady state of the atmosphere suppresses turbulence. The concept of the gravitational constant (g, 9.81 m/s^2) and temperature (θ) is introduced. Temperature is defined as the temperature at which a dry mass of a certain altitude moves adiabatically to a height of 1000 hpa. An increase in temperature with altitude means that the atmosphere is stable. Turbulence is also produced by mechanical convection at a rate proportional to $(\partial \overline{u}/\partial Z)^2$. The Richardson number can be said to be the ratio of these two processes, and is an indicator of thermal turbulence and atmospheric stability. The strong negative Richardson number characterizes strong vertical convection in an unstable atmosphere with dominant convection, and weak winds. As the mechanical turbulence increases, the Richardson number approaches zero as a neutral atmosphere $(\partial \overline{u}/\partial Z = 0)$. Finally, when the Richardson number becomes positive, vertical convective mixing ceases, and the atmosphere is stably stratified, resulting in mechanical turbulence.

$$S = \frac{g}{T}\left(\frac{\Delta \theta}{\Delta Z}\right) \tag{8}$$

$$\theta = T\left(\frac{p_0}{p}\right)^{0.286} \tag{9}$$

$$\text{Ri} = \frac{S}{(\partial \overline{u}/\partial Z)^2} = \frac{g}{T}\frac{(\partial \theta/\partial Z)}{(\partial \overline{u}/\partial Z)^2} = \frac{g}{T_0}\frac{(\partial/\partial Z)[\theta_0 + \theta_1]}{[(\partial/\partial Z)(u_0 + u_1)]^2} \tag{10}$$

2.5. WindSim

In the case of a mesoscale numerical model, modeling is carried out with a resolution of 1 to 10 km, but with this resolution, it is possible to obtain a numerical value close to reality in a system requiring high-resolution, such as a decrease in power generation due to a fluid flow in a complex terrain, or a wake effect at the rear of a turbine. It is difficult to determine, and accordingly, Computational Fluid Dynamics (CFD) models that can be modeled at a high resolution of tens to hundreds of meters are mainly used in wind farm design. WindSim, one of the computational fluid dynamics programs, is a program mainly used for site selection for wind farm construction, and was developed by WindSim A/S of Norway. The purpose of WindSim is to find an accurate solution of the flow characteristics generated as the wind passes through the turbine, taking into account all the natural properties of the fluid, such as compression, viscosity, friction, and turbulence. Since WindSim is a non-linear flow program, it can simulate special vortex phenomena, such as flow separation in complex terrain, much more accurately than a linear model. WindSim calculates pressure, wind speed, Turbulent Kinetic Energy (TKE), and turbulent dissipation rate using the Reynolds Averaged Navier–Stokes (RANS)

equation for each grid through the mesh system to calculate the flow field. The turbulence dissipation rate refers to the amount of energy transferred in the energy cascade process, in which large eddies are converted into several small eddies. In WindSim, Terrain creates a domain based on terrain elevation and roughness length, Wind Fields calculates a flow field using a turbulence model based on meteorological data, Objects can designate observation points and turbine locations, and flow value characteristics are identified. Six modules are sequentially performed: results that can confirm the results; wind resources that create an overall wind resource map; and energy that calculates annual power generation with wake effect applied. In other words, after analyzing the terrain data including the terrain height and roughness length in the Terrain module, the wind conditions in the corresponding domain are analyzed using the RANS equation through the Wind Fields module. Energy is calculated based on the wind resource map created after setting the location of the meteorological data and the coordinates to install the turbine with the Objects module. The Shuttle Radar Topography Mission (SRTM) 1″ (30 m) data provided by the National Aeronautics and Space Administration (NASA) was used for the topographical data of the wind resource map analysis area, and the ground roughness (Roughness length) was Vegetation Continuous Fields (VCF) data, the horizontal grid resolution of the domain is set to 120 m, and the total number of grids is 3,120,500. WindSim used in this study is ver. 11.0, and Table 4 shows the model settings.

Table 4. Input data and the configuration of WindSim SW.

Category	Value
X range [UTM coord.]	614,860.11–665,466.72
Y range [UTM coord.]	6,246,218.84–6,300,311.27
Refinement	None
Height distribution factor	0.1
Grid spacing [m]	120
Number of cells	3,120,500
Number of cells in the Z direction	20
Speed above boundary layer [m/s]	500
Height of boundary layer [m]	10
Turbulence model	Standard k-epsilon
Number of iterations	500

2.6. WRF

The Weather Research and Forecasting (WRF) model is a numerical weather forecasting (NWP) system developed by the US National Center for Atmospheric Research (NCAR) to meet both atmospheric research and operational forecasting requirements. WRF features two dynamic solvers, a data assimilation system, and a software architecture that allows for parallel computation and system scalability. This model can serve a wide range of meteorological applications over scales ranging from a few meters to thousands of kilometers. WRF allows researchers to create simulations that reflect real-world data (observation, analysis) or ideal atmospheric conditions. WRF provides two dynamic solvers for the calculation of atmospheric-governing equations, and variants of the model consist of WRF–ARW (Advanced Research WRF) and WRF–NMM (non-static intermediate-scale model).

2.7. Study Procedure

The purpose of this study is to improve the accuracy of the predicted power generation that can influence the economic feasibility of the offshore wind farm project. The first purpose is to secure basic research data that can analyze the characteristics of wind resources according to the atmospheric stability of the coast and the sea. The second purpose is to find out which wind speed calculation method, HHWS or REWS, brings results closer to the actual power generation. Finally, we try to find out what kind of temporal change in atmospheric stability occurs when the difference between the expected and the actual power generation is large, and whether or not sea surface temperature affects it. The results

of this study may not be readily applicable to other regions. This is because there are clear differences in the wind speed peak time, Weibull distribution, and turbulence characteristics of wind resources, depending on the northern or southern hemisphere, latitude, climate, and coastline shape. First, the Anholt wind farm is implemented through WindSim, and HHWS and REWS are calculated in 10 min units through offshore LiDAR observation data. These data are input into WindSim to calculate each expected power generation, and time-series comparison analysis is performed with the actual power generation recorded in SCADA. This calculates the error rate with the actual power generation, and analyzes it in relation to the atmospheric stability when the error rate is large or small. However, since the temperature data on LiDAR is only one month in two years, the temperature data are secured through WRF simulation using ERA5 data. Although these results cannot be applied to all offshore wind farms, we are conducting this study because we believe that a good database can be established only when many of these research results are introduced and accumulated. Figure 4 shows the detailed research procedure.
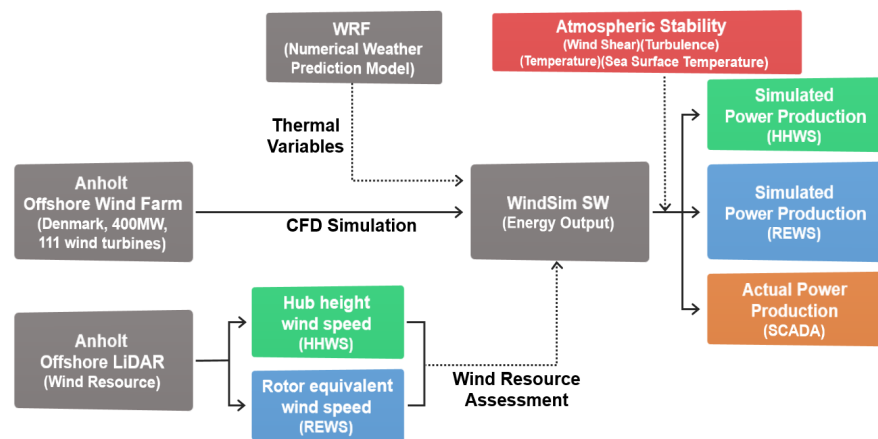

Figure 4. Introduction to our research procedures and methodologies.

3. Results

3.1. Model Simulation

In this study, simulation tools called WindSim and WRF were used, and WindSim was used to analyze wind resources by HHWS and REWS, and calculate predicted power generation. WRF is used to calculate the thermal atmospheric stability, which affects the amount of wind power generation. Temperature, sea surface temperature, or heat flux values are required to obtain the thermal atmospheric stability. The only temperature observed from marine LiDAR were data for the month of December 2014 out of two years (a few percent of data acquisition rate, compared to the entire period). Therefore, ERA5 re-analysis data were used for MCP from the temperature point of view, and correlation with the observed values was analyzed with temperature data in December 2014 to verify ERA5 (Figure 5).

For correlation analysis, root mean square error (*RMSE*), mean bias error (*MOE*), and index of agreement (*IOA*) indicators were used, and the equations for each indicator are as follows:

$$RMSE = \sqrt{\frac{\sum_{i=1}^{n}(M_i - O_i)^2}{n}} \tag{11}$$

$$MBE = \frac{\sum_{i=1}^{n}(M_i - O_i)}{n} \tag{12}$$

$$IOA = 1 - \left[\frac{\sum_{i=1}^{n}(O_i - M_i)^2}{\sum_{i=1}^{n}(|M_i - \overline{O}| + |O_i - \overline{O}|)^2}\right] \tag{13}$$

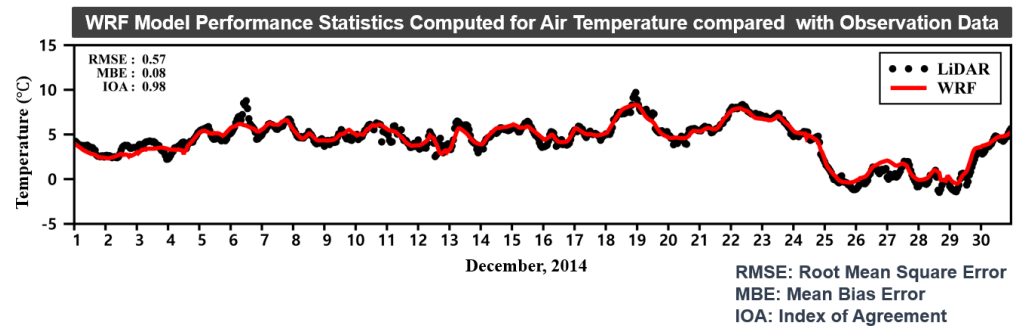O : *Observation data*, M : *Model output*

Figure 5. Time-series trends of LiDAR air temperature observation data and ERA5-based WRF analysis data in December 2014.The black dots are the LiDAR observation data, and the red solid line is the WRF simulation result (RMSE: 0.57, MBE: 0.08, IOA: 0.98).

As a result of analyzing the one-hour average temperature data of 10 m for the month of December 2014, RMSE, MOE, and IOA were (0.57, 0.08, and 0.98), respectively, showing a significant level of correlation. Although LiDAR observation data are used for wind resource analysis, wind speed correlation was also analyzed to further improve the reliability of the ERA5 temperature data, compared to the actual observation value. Since it is clear that temperature-related changes in the thermal properties in the atmospheric boundary layer will affect the changes in wind resources, the wind speed data of ERA5 were also compared with the observed values. Similarly, we compared only the month of December 2014, which was the same as the period for securing temperature data, and the RMSE, MOE, and IOA of wind speed data at 65 m of (1.46, −0.45, and 0.97), at 85 m of (1.45, −0.40, and 0.97), and at 141 m of (1.47, −0.35, and 0.97), respectively, were confirmed (Figure 6).
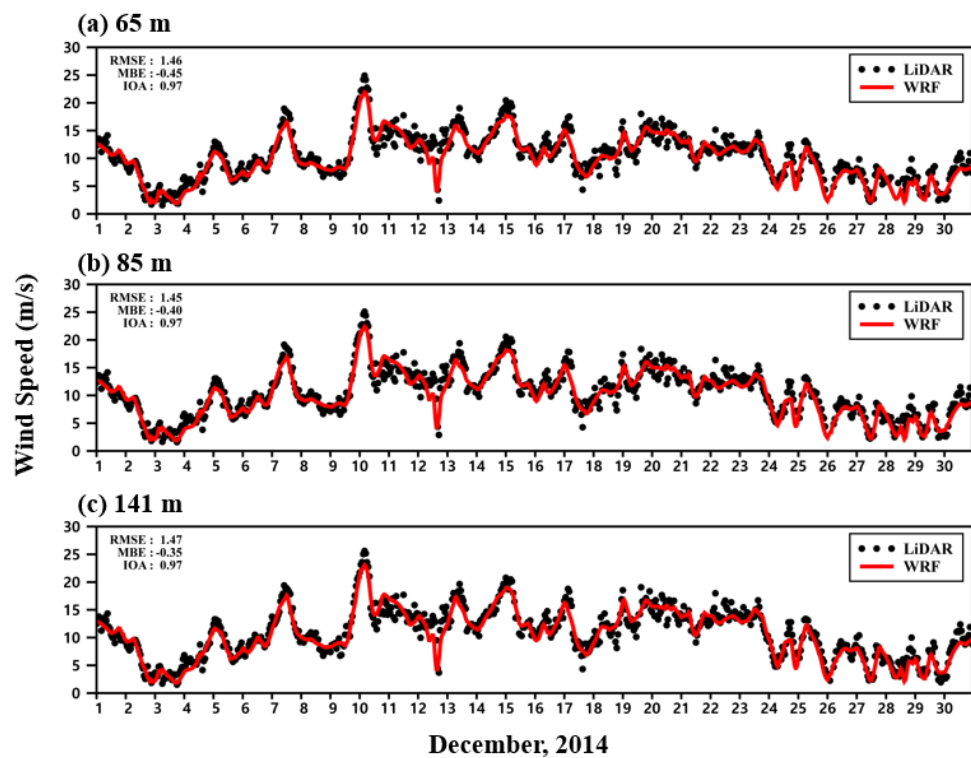

Figure 6. Time-series trend of wind speed LiDAR observation data by each height in December 2014 and WRF analysis data based on ERA5. The black dots are the LiDAR observation data, and the red solid line is the WRF simulation result. The analysis results are (65, 85, and 141) m from the top, respectively (65 m: RMSE: 1.46, MBE: −0.45, IOA: 0.97/85 m: RMSE: 1.45, MBE: −0.40, IOA: 0.97/141 m: RMSE: 1.47, MBE: −0.35, IOA: 0.97).

WindSim also showed CFD analysis results that converge in all 12 sector analyses at 30-degree intervals. It seems that no problems occurred in the process of calculating wind speed, wind direction, Weibull distribution, turbulence intensity, turbulent kinetic energy, and wake loss rate (Figure 7).
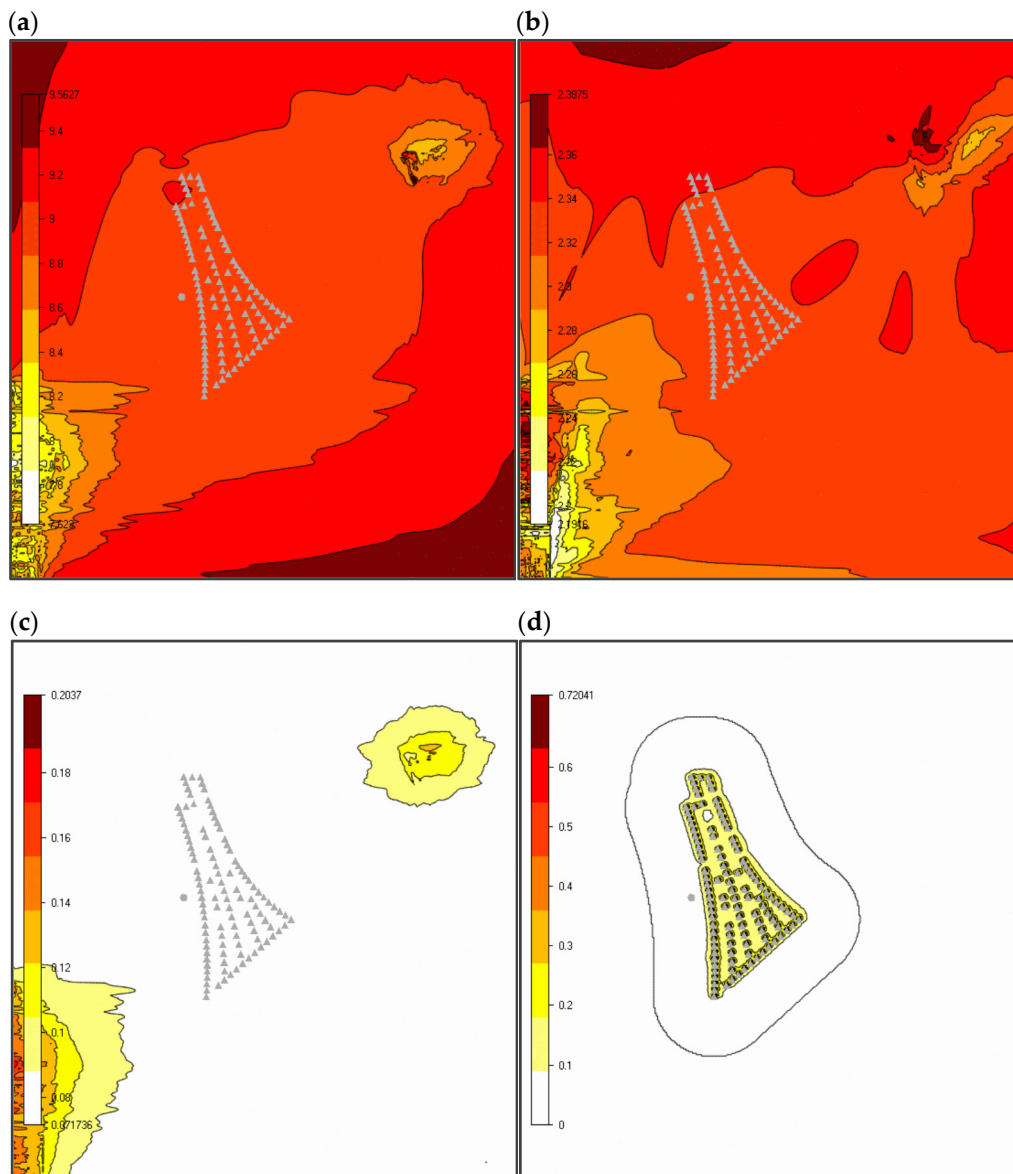

Figure 7. WindSim simulation results for the Anholt offshore wind farm: (**a**) wind speed at 105 m; (**b**) Weibull shape factor; (**c**) turbulence intensity; and (**d**) wake dissipation rate.

3.2. Stream Sector and Data Filtering

In accordance with IEC 61400-12-1 Annex A, major buildings and wind turbines affecting the vicinity of meteorological masts and wind turbines were selected as major obstacles. As explained in Section 2.1, the analysis was performed on only the 5 wind turbines located on the windward side of the 111 wind turbines of the Anholt offshore wind farm (A01, A02, A03, B01, and C01 wind turbines). To set the effective measurement azimuth of the wind direction, the wind direction affected by the nearby wind turbines was determined by the location (separation distance, angle) between the turbines. Accordingly, the distortion azimuth that should be excluded from the effective measurement azimuth due to the wake effect from the adjacent wind turbine was calculated using Equation (14). However, to check the sensitivity of the analysis result to the wake effect, the wake effect

cannot be completely excluded, so the main wind direction of the offshore LiDAR was commonly applied, despite the calculation of the effective azimuth for each turbine. In this case, only bins corresponding to 3.5% or more of the frequency of wind speed occurrence at 1-degree intervals were extracted, and wind directions from (94 to 288) degrees were selected (Figure 8).

$$\alpha = 1.3 \, Arctan\left(\frac{2.5D_n}{L_n} + 0.15\right) + 10 \tag{14}$$

α : Disturbed sector
D_n : Rotor diameter at neighborhood wind turbine
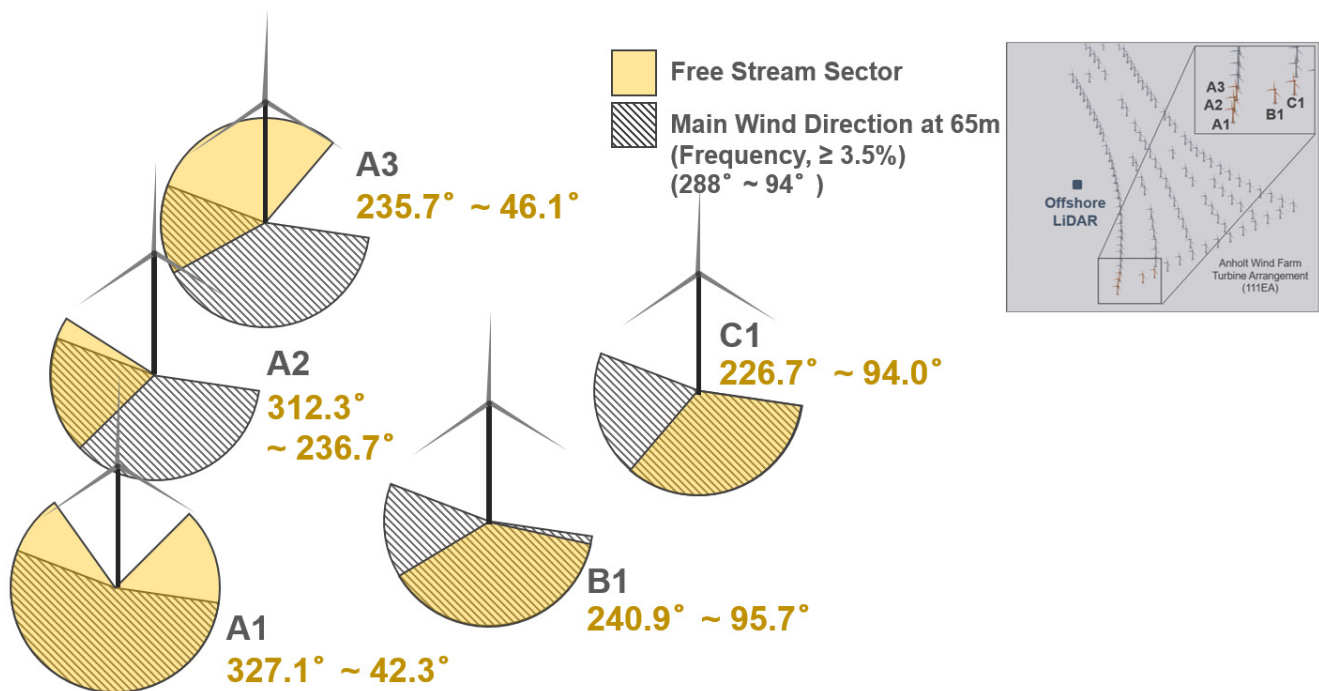L_n : Distance between neighborhood wind turbine and target wind turbine

Figure 8. Free stream sector angle (yellow) for each turbine to be analyzed within the Anholt offshore wind farm and the main wind direction of the entire offshore wind farm (gray hatched line). The free stream sector refers to the wind direction free from wake effects by the surrounding turbines.

Data filtering consisted of a total of 4 steps. First-order filtering was performed for the effective azimuth introduced above. Second-order filtering was performed on the section containing missing values. The third and fourth orders are filtering for wind speed and power generation, respectively. In the third phase, the section with 0 power generation was filtered, despite the inflow of wind corresponding to the operating wind speed of the wind turbine (>3.5 m/s). Lastly, in the fourth step, filtering was performed for the section less than the cut in wind speed of the wind turbine. The analysis was performed by selecting the time when the data of all turbines are valid at the same time. Finally, about 41% of the total raw data was used for analysis. Table 5 shows the data filtering rate and filtering items.

Table 5. Data filtering categories and data availability before and after the data filtering at each turbine.

SCADA Data Filtering Category	Wind Turbine									
	A01		A02		A03		B01		C01	
Valid Data (#, %)	Data	%	Data	%	Data	%	Data	%	Data	%
Pre-Filtered Data	104,584	100.0	104,584	100.0	104,584	100.0	104,584	100.0	104,584	100.0
Wind Direction	71,563	68.4	71,563	68.4	71,563	68.4	71,563	68.4	71,563	68.4
(All) Wind Direction	71,563 (68.4%)									
Missing Value	102,958	98.4	104,318	99.7	104,559	99.9	104,216	99.9	104,480	99.9
(All) Missing Value	102,195 (97.7%)									
Cut in Speed, but Power ≤ 0	100,102	95.7	101,588	97.1	103,454	98.9	102,016	97.5	102,343	97.8
(All) Cut in Speed but No Power	91,113 (89.1%)									
Below Cut in Speed	95,031	90.8	103,162	98.6	104,164	99.6	103,892	99.3	104,178	99.6
(All) Below Cut in Speed	92,091 (88.0%)									
Post-Filtered Data	55,902	53.4	66,879	63.9	69,988	66.9	67,935	64.9	68,812	65.8
All (Post Filtered Data)	43,507 (41.6%)									

3.3. Comparison with Actual Data

3.3.1. Rotor Equivalent Wind Speed Calculation

In this study, the rotor disk was divided into a total of 5 sectors to calculate the rotor equivalent wind speed, and Figure 9 and Table 6 show the area and height of the detailed sectors. Table 1 mentions that the hub height of the turbine is 81.6 m, and Table 2 explains that the height of the offshore platform where the LiDAR is installed is 25.6 m above sea level. For convenience in calculation, the turbine hub height and LiDAR observation height offset are assumed to be 80 and 25 m, respectively. Although the uncertainty of the analysis result may increase slightly, it was judged that it would not have a significant level of influence on the result.
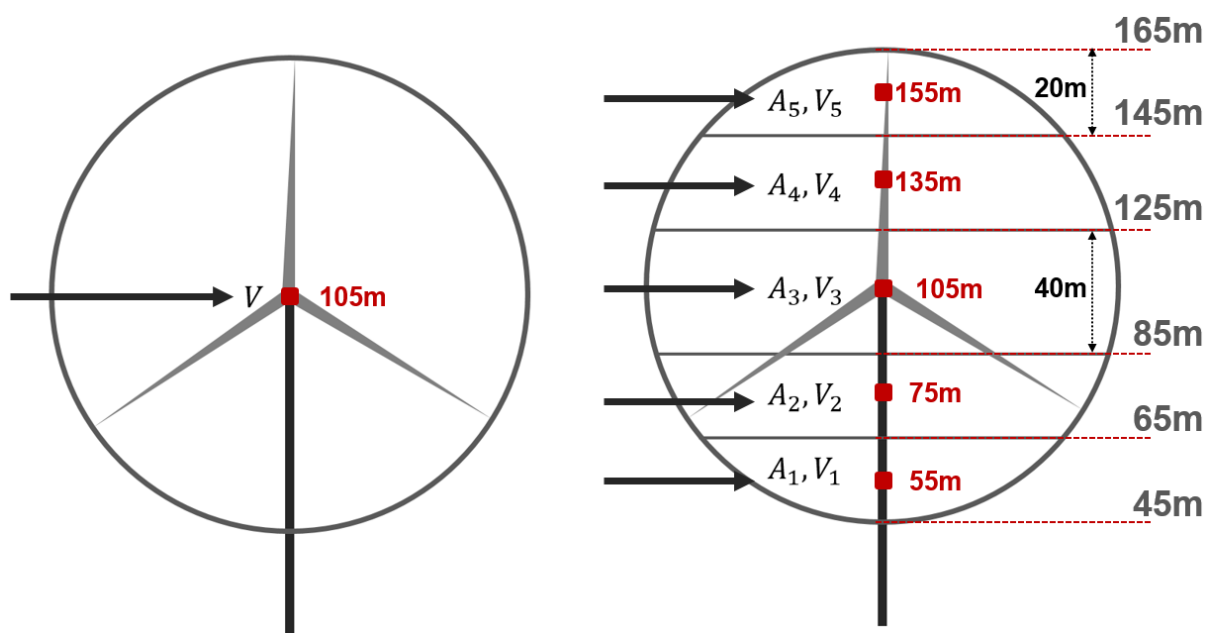

Figure 9. HHWS method (**left**) and REWS method (**right**) compared in this study. The rotor disk is divided into 5 sub-sectors, and only the middle sector near the hub height is set at 40 m in height.

Table 6. Detailed data summary at sub-sectors for calculating the rotor equivalent wind speed.

Sector	Wind Speed Height [m]	Wind Speed [m/s]	Segment Weighting [%]	Segment Bottom Height [m]	Segment Upper Height [m]	Segment Height [m]
A5	155	9.68	10.96	45	65	20
A4	135	9.36	18.22	65	85	20
A3	105	9.05	41.64	85	125	40
A2	75	8.59	18.22	125	145	20
A1	55	8.16	10.96	145	165	20

3.3.2. Comparison between HHWS and REWS

After inputting the observation values of wind resources for HHWS and REWS into WindSim, respectively, the generation amount of the Anholt offshore wind farm for two years was calculated. The wind speed values for each wind turbine simulated in WindSim and the wind speed values for each wind turbine recorded in SCADA were compared. A correlation analysis was performed between the simulated wind speed and the actual value at the location where the analysis target turbine was installed (Figure 10). On average, regardless of HHWS and REWS, the correlation between the simulated value and the actual wind speed value was 0.8 or higher. The correlation between REWS and the actual SCADA wind speed was slightly higher than that of HHWS, but there was no significant difference (Table 7). In the simulated wind speed values, REWS showed a slightly higher wind speed value than HHWS.

Table 7. Correlation coefficient (R^2) between simulated wind speed and actual SCADA wind speed at each wind turbine location.

Correlation (R^2)	Turbine A01	Turbine A02	Turbine A03	Turbine B01	Turbine C01
Actual Wind Speed vs. HHWS	0.815	0.821	0.820	0.814	0.787
Actual Wind Speed vs. REWS	0.816	0.824	0.821	0.817	0.791

Meanwhile, the wind speed difference distribution was expressed in ArcGIS using the wind resource grid values of REWS and HHWS calculated by WindSim. In the vicinity of the offshore wind farm, REWS showed a high distribution of about 0.1 m/s. Considering that the main wind is a westerly wind, it can be seen that the wavy contours are stacked on the right side of the offshore wind farm. It appears that the wake effect in the wind farm is reflected, and it is judged that as the wind passes through the wind farm, the difference between REWS and HHWS slightly increases.

In the vicinity of the mainland located in the southwest of the analysis domain and Anholt Island located in the northeast of the analysis domain, shades of blue are shown. These indicate that the difference between REWS and HHWS is small compared to other regions, and it seems that the difference between REWS and HHWS is smaller due to the length of roughness on land being higher than at sea (Figure 11).
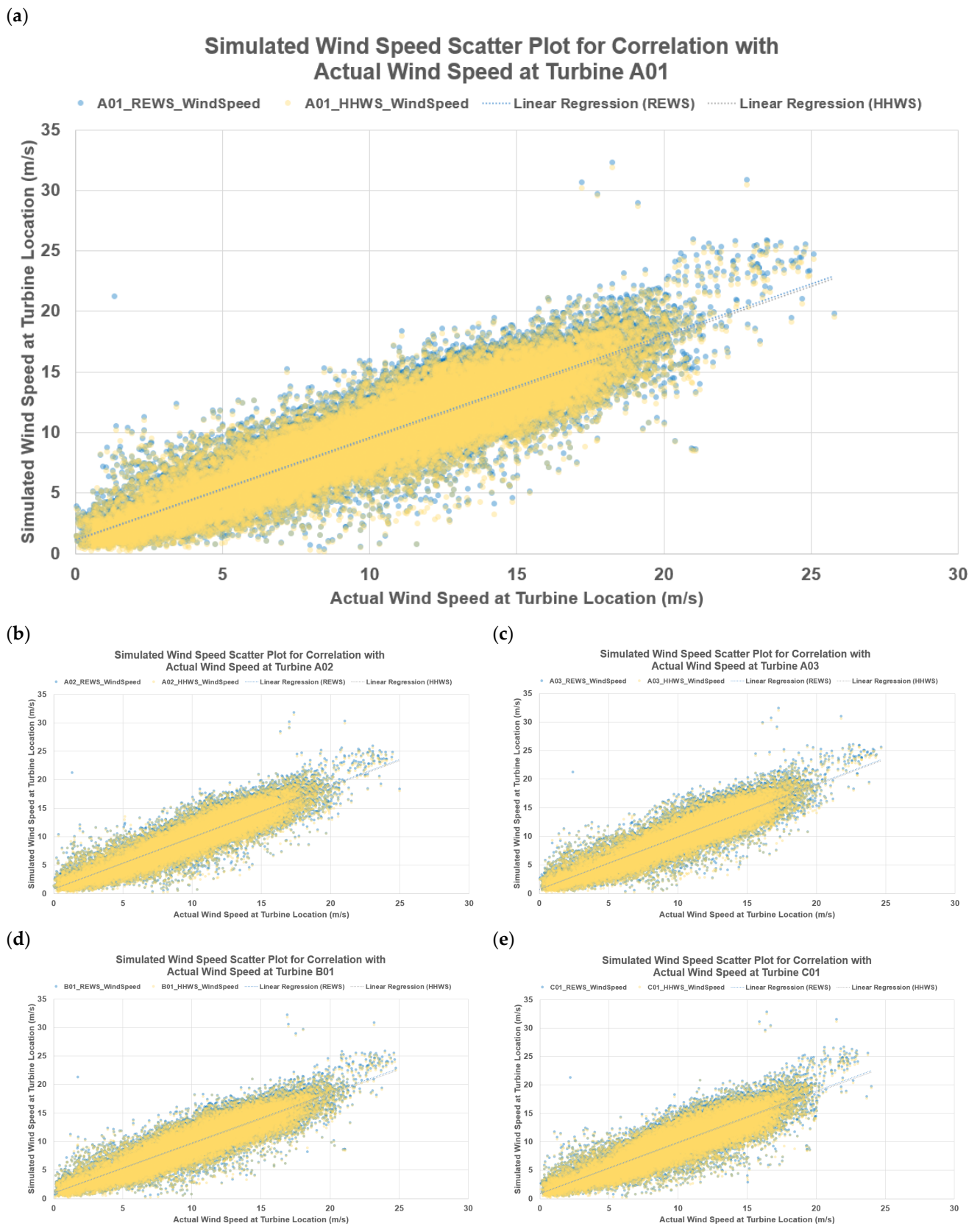
(**a**)

(**b**)

(**c**)

(**d**)

(**e**)

Figure 10. Correlation analysis through scatterplot distribution between simulated wind speed and actual SCADA wind speed at each wind turbine location: (**a**) A01; (**b**) A02; (**c**) A03; (**d**) B01; and (**e**) C01 wind turbine.
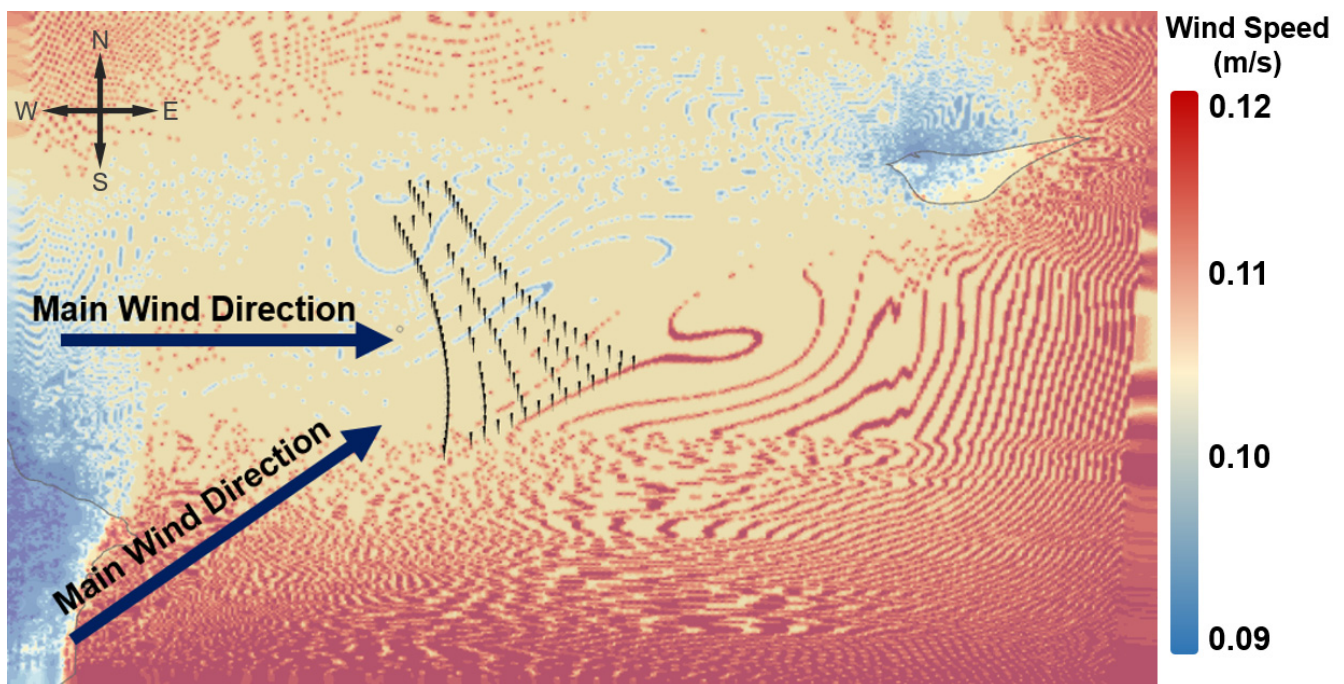
Figure 11. Wind speed difference distribution of REWS and HHWS within the research domain including the Anholt offshore wind farm. The closer to red, the greater the wind speed difference.

3.3.3. Comparison with Power Output

The scalar difference and trend of HHWS and REWS compared to SCADA actual wind speed by time of day were compared. At the same time, the predicted generation using HHWS and REWS was also compared to the actual generation. Figure 12 shows the trend of daily wind speed and power generation for each turbine. The gray solid line and bar indicate the wind speed and power generation of SCADA, respectively. Red and blue represent HHWS and REWS, respectively. In the time-series analysis, the difference between the wind speed at the turbine location input to SCADA and the wind speed simulated by WindSim was significant. Clearly, the diurnal trend seems to coincide without any major problem, but the absolute value difference is up to 0.47 m/s. The actual wind speed of the turbines A02 and A03 was similar to that of the REWS, but unfortunately, the wind turbines A01, B01, and C01 located in a straight line showed a large error in relation to the simulated wind speed. It is necessary to sufficiently check whether the WindSim software does not simulate the wind speed at each wind turbine location well, or whether special weather phenomena at the site where the wind speed is amplified are overlapped.

When only looking at the average wind speed and daily change, REWS showed a consistently higher value compared to HHWS. This eventually seems to imply that REWS is closer to SCADA wind speed, but REWS generation accuracy was not dominant at all time-points. The daily change graph shows the error rate of the expected generation of HHWS and REWS, compared to the actual generation. The data of the five wind turbines to be analyzed were averaged, and the error rate was calculated by subtracting each simulated power from the actual power generation, and dividing by the actual power generation (Figure 13). Through this formula, a positive error rate means that the simulated power generation is smaller than the actual power generation, and a negative number indicates that the simulated power generation is greater.

As Table 8 clearly shows, it seems that there are times when the REWS-based generation forecast is more accurate, and there are times when the HHWS-based generation amount is rather more accurate. In more than half of the day, the REWS-based simulated power generation showed a higher value than the actual power generation. In particular, it showed a pattern of simulating a value that was consistently higher than the actual power

generation from 14:00 until sunrise. On the other hand, HHWS simulated a relatively small amount of power generation, compared to the actual power generation. A slightly higher power generation was simulated 2–3 h before and after sunset, but lower values than the actual power generation were simulated in other sections. To find out whether such a result is overestimated or underestimated compared to the actual power generation, the absolute value difference with the actual power generation was calculated. Among REWS and HHWS simulated power generation, the section with a smaller error with actual power generation is indicated in yellow in Table 4. From midnight to 14:00, most of the REWS simulated power generation was close to the actual power generation. On the other hand, from 15:00 to 21:00, the HHWS simulated power generation was closer to the actual power generation. The maximum release time of heat flux from the land surface with low specific heat is 14 h, whereas the time for heat flux emission from the ocean with high specific heat is delayed. This is because the ocean can retain more heat, and do so longer. The time when the REWS-based simulated power generation and the actual power generation error increases is from 15:00 to 21:00, which is generally the time when the heat flux from the ocean is released. The release of thermal energy from the ocean appears to change the magnitude or shape of wind shear or thermal convection, and these movements appear to affect REWS.
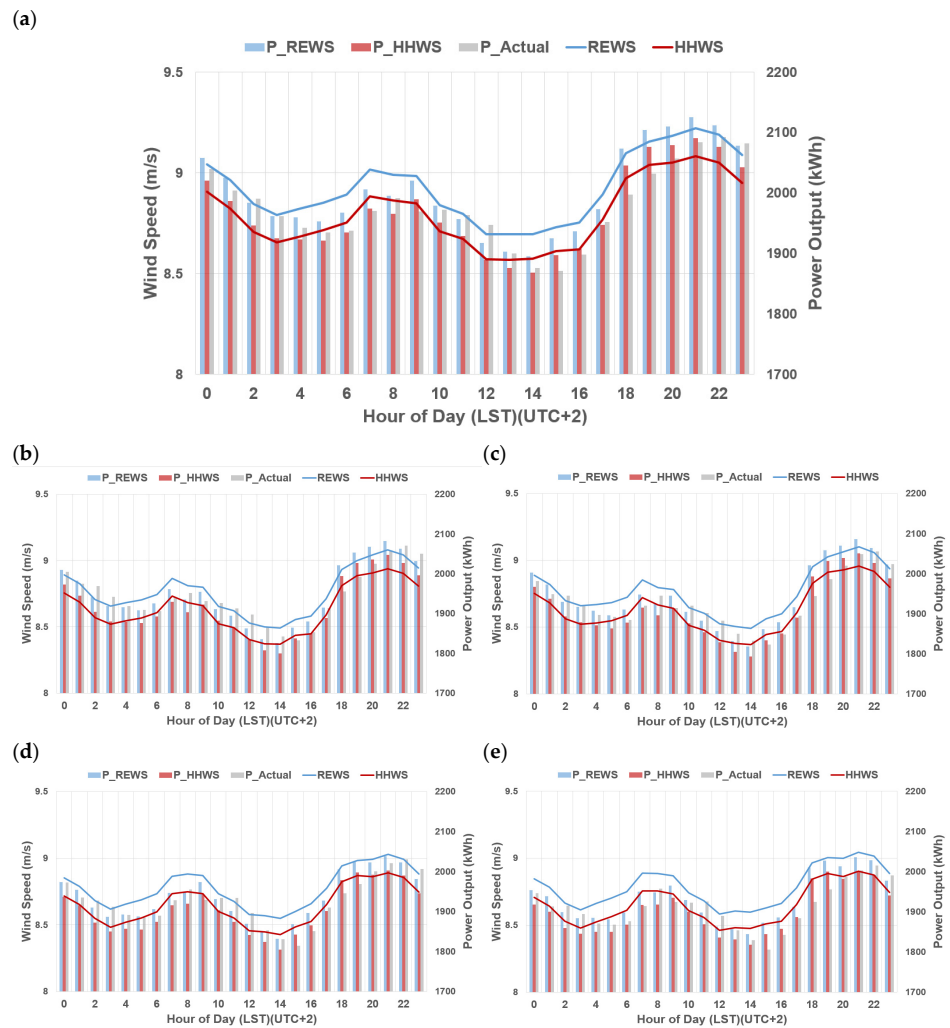

Figure 12. Comparison of the wind speed/power output at each turbine location simulated by REWS and HHWS, and the SCADA actual data: (**a**) A01; (**b**) A02; (**c**) A03; (**d**) B01; and (**e**) C01 wind turbine. Blue colored solid line and stick represent REWS, while red colored solid line and stick mean HHWS, and gray colored solid line and stick mean SCADA data.
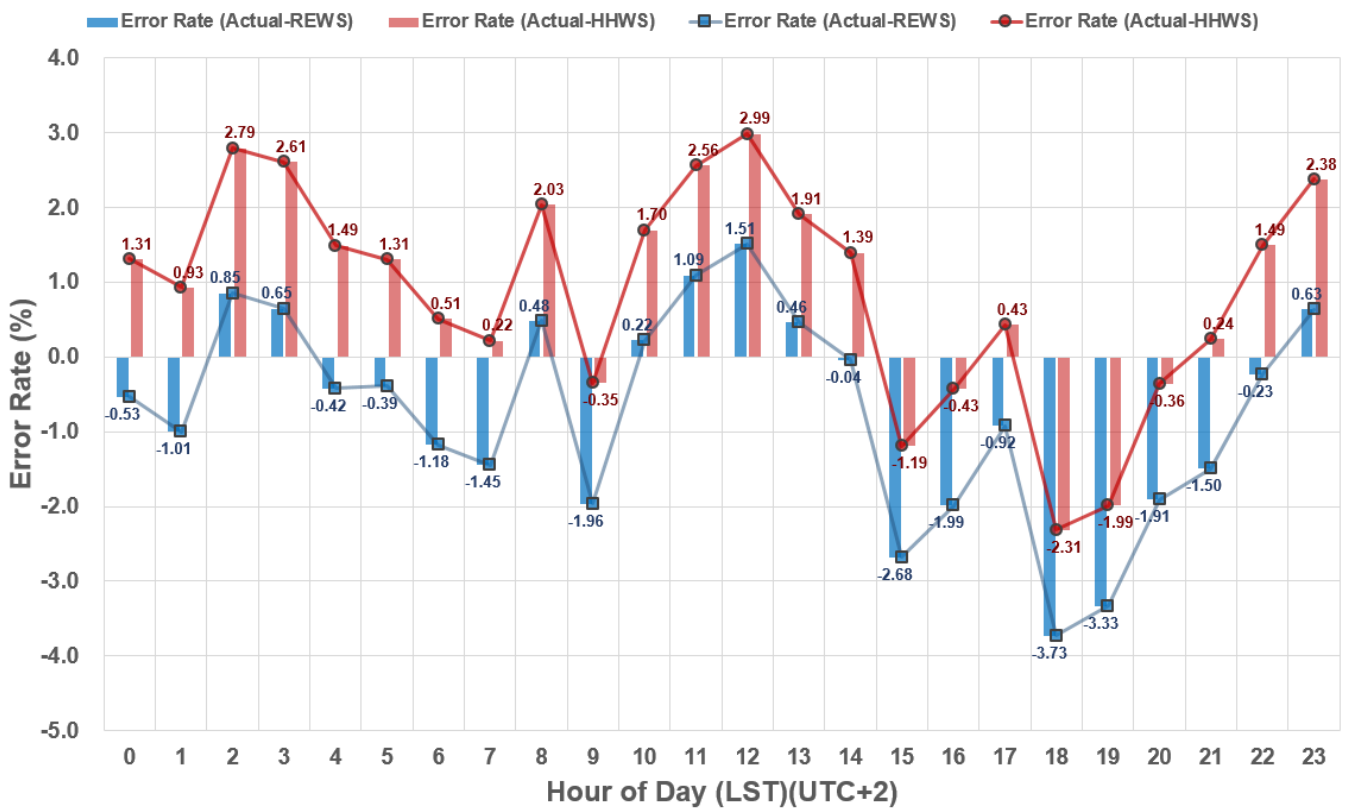
Figure 13. Changes in diurnal hourly error rate of the REWS-based and HHWS-based simulated power output, compared to the actual power output. The red bar shows the error between the actual power output and the HHWS-based power output, while the blue bar shows the error with the REWS. If the error rate is positive, this means that the actual power output is higher than the simulated power output.

Table 8. The distribution of simulated wind speed when the simulated power output is higher than the actual power output, and the absolute difference with the actual power output is smaller.

Time (LST)		0	1	2	3	4	5	6	7	8	9	10	11	12	13	14	15	16	17	18	19	20	21	22	23
>Actual Power	REWS	•	•			•	•	•	•		•					•	•	•	•	•	•	•	•	•	•
	HHWS										•					•	•			•	•	•			
Abs. Diff.	REWS	▓		▓	▓	▓		▓		▓	▓		▓	▓	▓	▓								▓	▓
	HHWS		▓				▓	▓		▓			▓	▓	▓	▓	▓	▓	▓	▓	▓	▓			

Yellow colored box represents the method with more accurate power due to less error compared to the actual power output.

To see monthly changes rather than annual averages, we examine the characteristics of November, December, and January, when the temperature is generally low, and the trends in May, June, and July, when the temperature is high. In Figure 14, the solid red line is the error between the actual power generation and the HHWS-based simulated power generation, while the blue line is the REWS-based result. The gray solid line represents the wind speed difference between REWS and HHWS. In the season when the temperature is low, the variation in the error rate between the simulated power generation and the actual power generation amount does not appear to be significant. Additionally, the error rate between the simulated power generation of HHWS and REWS does not appear to show a significant difference. The difference in wind speed between REWS and HHWS decreases in the afternoon, which is the same in the low and high seasons. However, in the season of high temperature, the generation error rate shows a completely different pattern.

Compared to the low temperature season, the generation error rate changed significantly according to the time of day, and there were times when the same trend did not appear.
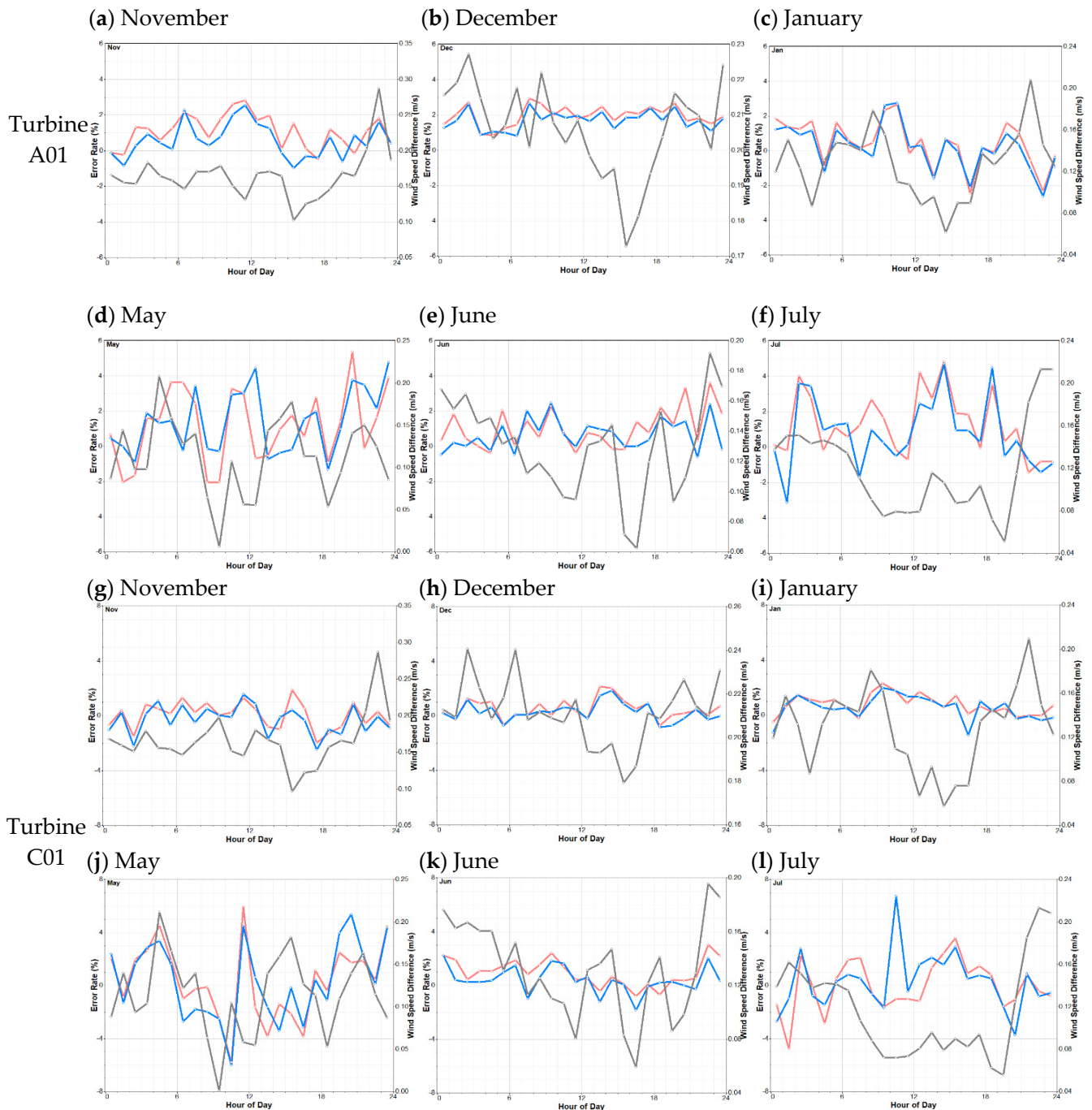
(a) November   **(b)** December   **(c)** January

Turbine A01

(d) May   **(e)** June   **(f)** July

(g) November   **(h)** December   **(i)** January

Turbine C01   **(j)** May   **(k)** June   **(l)** July

Figure 14. Monthly error rates of simulated power output based on REWS (Blue) and HHWS (Red) and the actual power output, and the distribution of wind speed differences between REWS and HHWS (Gray). These are the analysis data for turbines A01 and C01, respectively, and November, December, and January, which are close to winter, and May, June, and July, which are close to summer, are analyzed, respectively.

3.4. Atmospheric Stability in Anholt OWF

To find out how the error with actual power generation was related to changes in atmospheric stability in the atmospheric boundary layer, first, the atmospheric stability distribution characteristics in the vicinity of the Anholt offshore wind farm were analyzed.

As explained in Section 2.4, atmospheric stability in this study was analyzed based on wind shear, turbulence intensity, and Richardson number. All atmospheric stability indicators were classified into five states according to the criteria in Table 3 (strong unstable, unstable, neutral, stable, and strong stable).

First, atmospheric stability analysis based on wind shear was performed. Figure 15 shows the result of air stability classification after calculating the wind shear coefficient from wind speed data at (40 and 116) m (the y-axis altitude in the figure is the corrected value offset by 25 m from the offshore platform). When the vertical wind speed profiles are classified by atmospheric stability, it is clear that the more unstable the atmosphere, the smaller the difference in wind speed between the upper and lower layers, and sometimes the wind speed in the upper layer is smaller than that in the lower layer. Based on offshore LiDAR observations, the wind shear standard atmospheric stability in the vicinity of the Anholt offshore wind farm can be said to be unstable or neutral (average wind shear coefficient of 0.11). In general, atmospheric stability is expressed as neutral when the wind shear coefficient is 0.143, according to the 1/7 rule in micrometeorology.
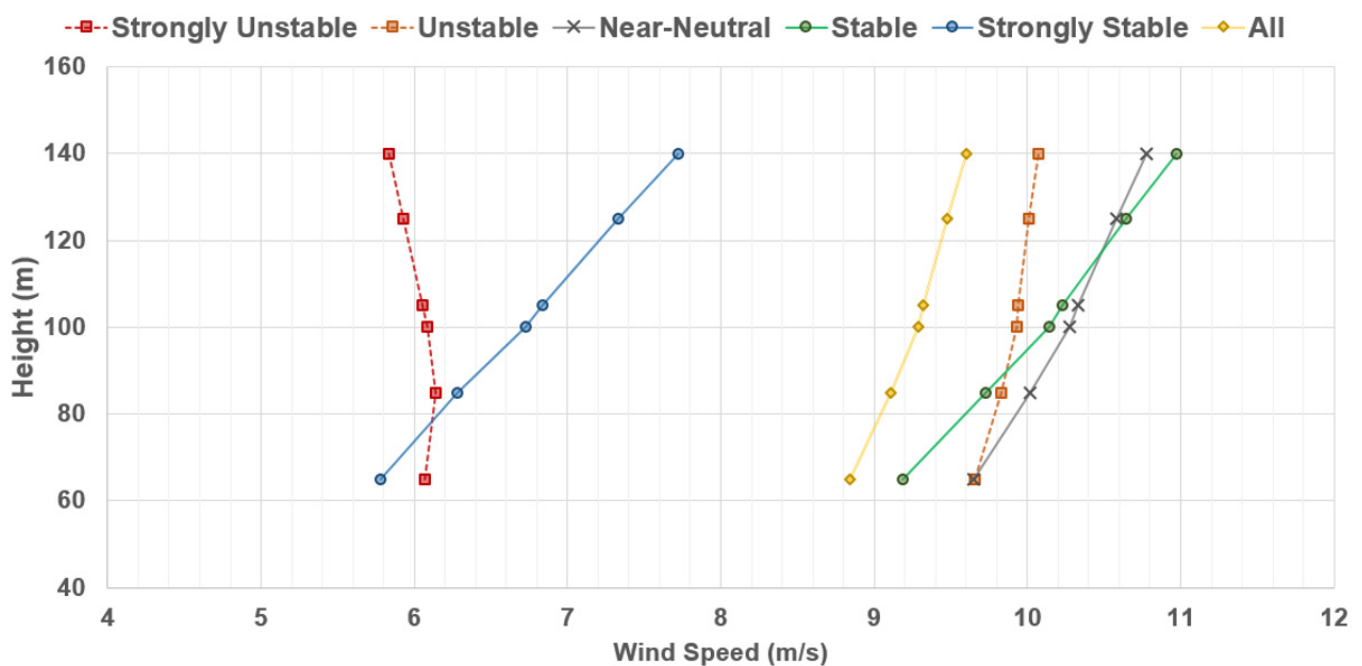

Figure 15. Wind shear-based vertical wind speed profile types for each atmospheric stability using two-year observation data from Anholt offshore LiDAR. Red square, orange square, gray cross, green circle, and blue circle represent strongly unstable, unstable, near-neutral, stable, and strongly stable, respectively. Yellow diamond represents the all-averaged vertical wind speed profile.

Figure 16 confirms the changes in the daily wind shear coefficient and the distribution of the appearance frequency of atmospheric stability. The detailed wind shear changes in the rotor disk reveal why an error can be made by considering only the hub altitude and wind speed. It can be predicted that various wind shear coefficients and changes with time will affect the load and torque of the turbine, including the blades. This can be a major cause of the increase or decrease in the amount of power generation.
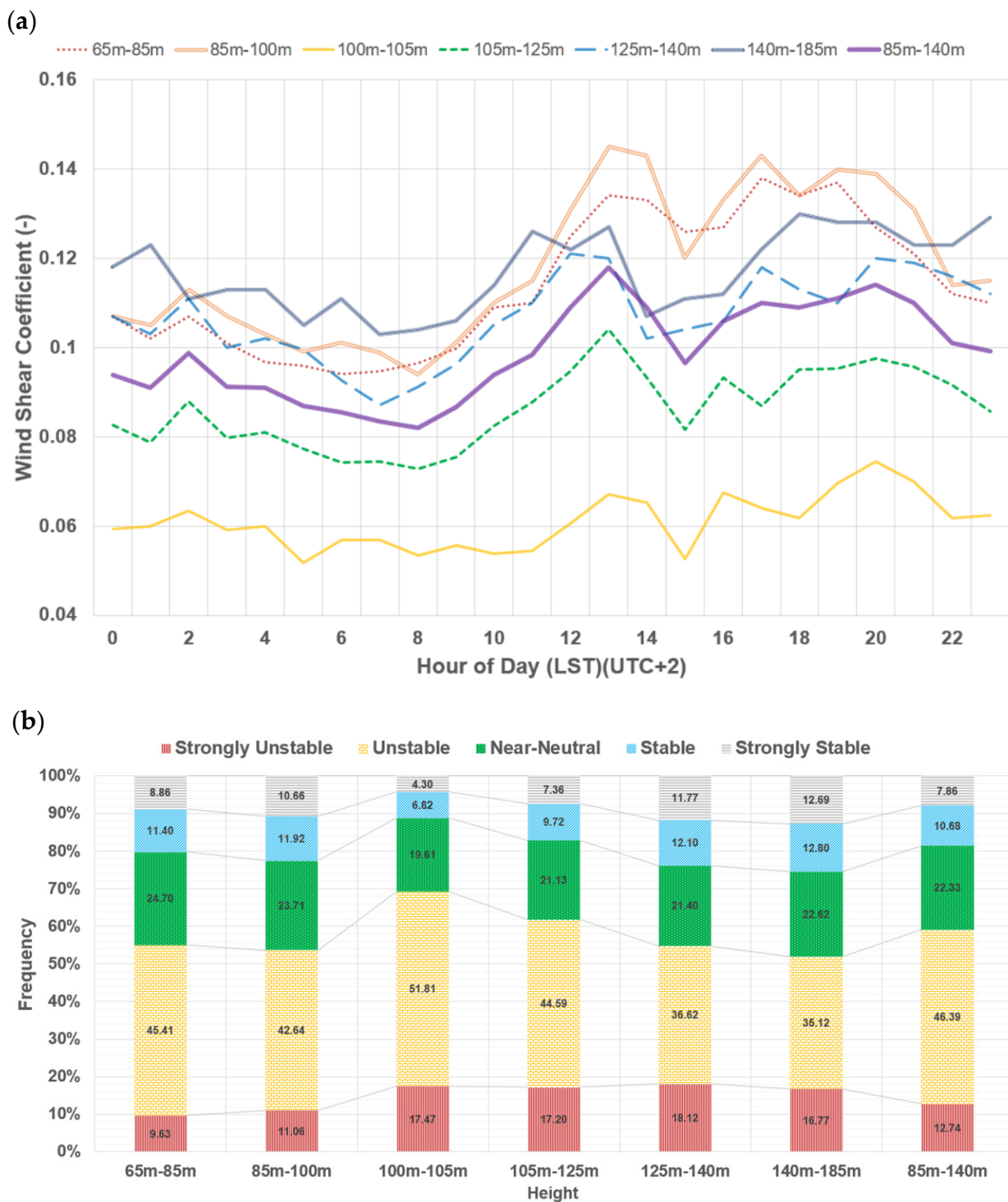
Figure 16. (**a**) Daily change in wind shear coefficient, and (**b**) atmospheric stability frequency distribution ratio for each height. Wind shear coefficient between (85 and 140) m has a distribution of (0.08–0.12), and atmospheric stability is unstable or near-neutral.

The second is the classification of atmospheric stability according to the intensity of turbulence. Figure 17 derives cross-section analysis results for wind speed and turbulence intensity at the Anholt offshore wind farm. Analysis was performed on the part marked with a white solid line in the domain of the offshore wind farm displayed in the upper right corner. It can be said that the longitude range corresponding to the horizontal axis of each figure coincides with the white solid line indicated in the domain. The upper part in

Figure 17 shows the wind speed and turbulence intensity in the northern part of the wind farm, where the distance between the offshore wind turbines is dense. On the other hand, the lower part of Figure 17 is the southern part of the offshore wind farm close to where the five wind turbines to be analyzed are located. The results of the northern part of the wind farm show that the turbulence intensity is weak at longitudes lower than 11 degrees, because the wind has not yet passed through the wind farm, but it can be confirmed that as the hardness exceeds 11 degrees, the intensity of turbulence increases. This was more evident at the lower altitude than the hub altitude. A more rapid increase in turbulence intensity was confirmed in the southern part of the wind farm, which is believed to be because the main wind directions are westerly and southwesterly winds. This is because the wake effect caused by the wind turbine on the windward side overlaps at the same time as the southwesterly wind series wind blows. As such, it can be seen that the intensity of turbulence increases on penetrating the wind farm.
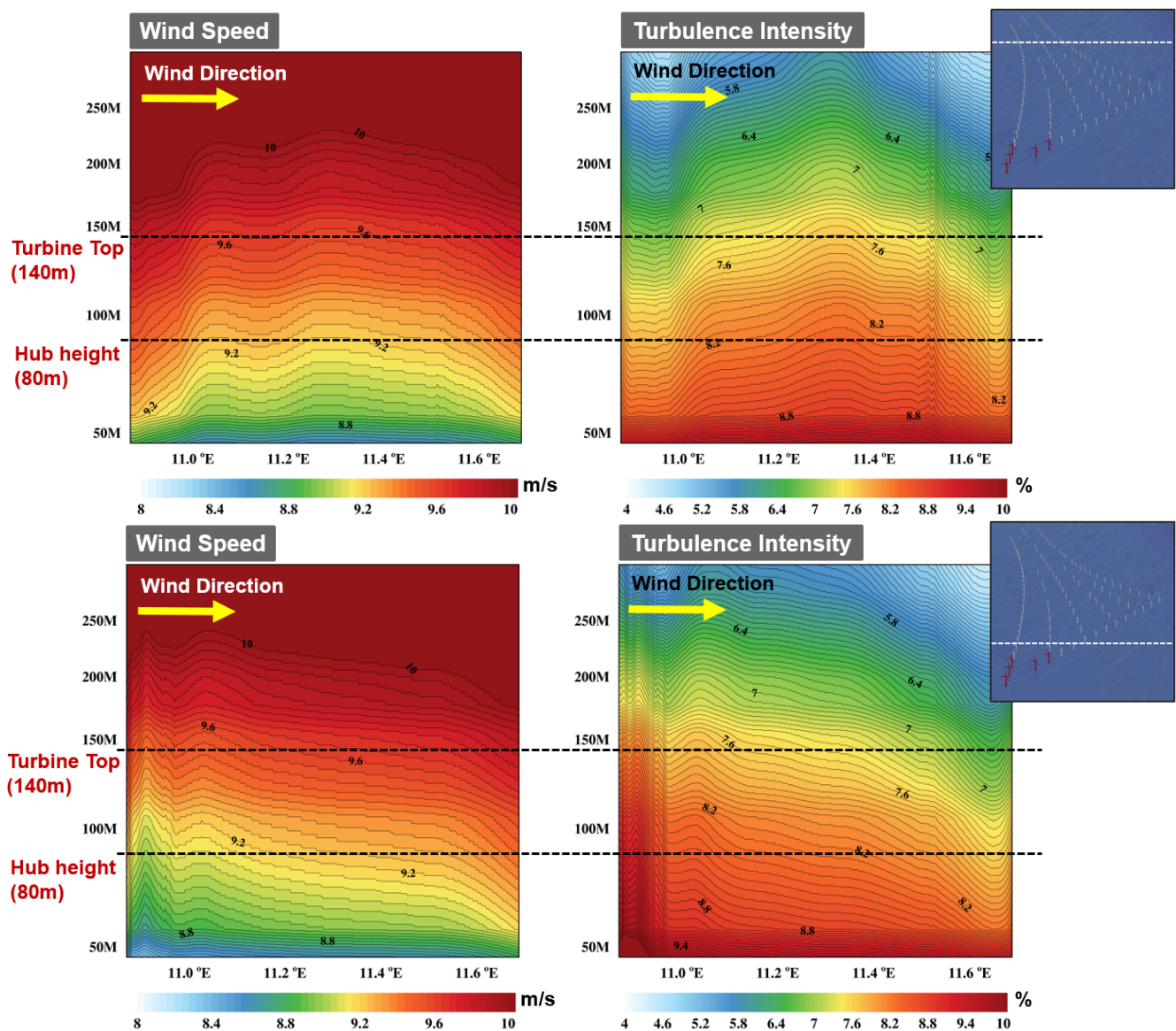

Figure 17. Cross-sectional analysis of wind speed and turbulence intensity by latitude at the Anholt offshore wind farm. The distribution of wind speed and turbulence intensity from (50 to 300) m above Mean Sea Level (MSL) can be checked. The black dashed lines indicate the hub height (80 m) and the uppermost part of the rotor disk (140 m) of the wind turbine, respectively.

Figure 18 confirms the daily turbulence intensity change by altitude. The intensity of turbulence was highest at 65 m, the lowest point, and peaked at 10 a.m. It showed a general change curve in which the intensity of turbulence decreased at sunset, and increased after sunrise. On the other hand, unlike wind shear-based atmospheric stability classification, atmospheric stability based on turbulence intensity showed a generally stable state. At each altitude, the unstable atmosphere was less than 20%, indicating that more than 60% was a stable atmosphere.

(**a**)

(**b**)
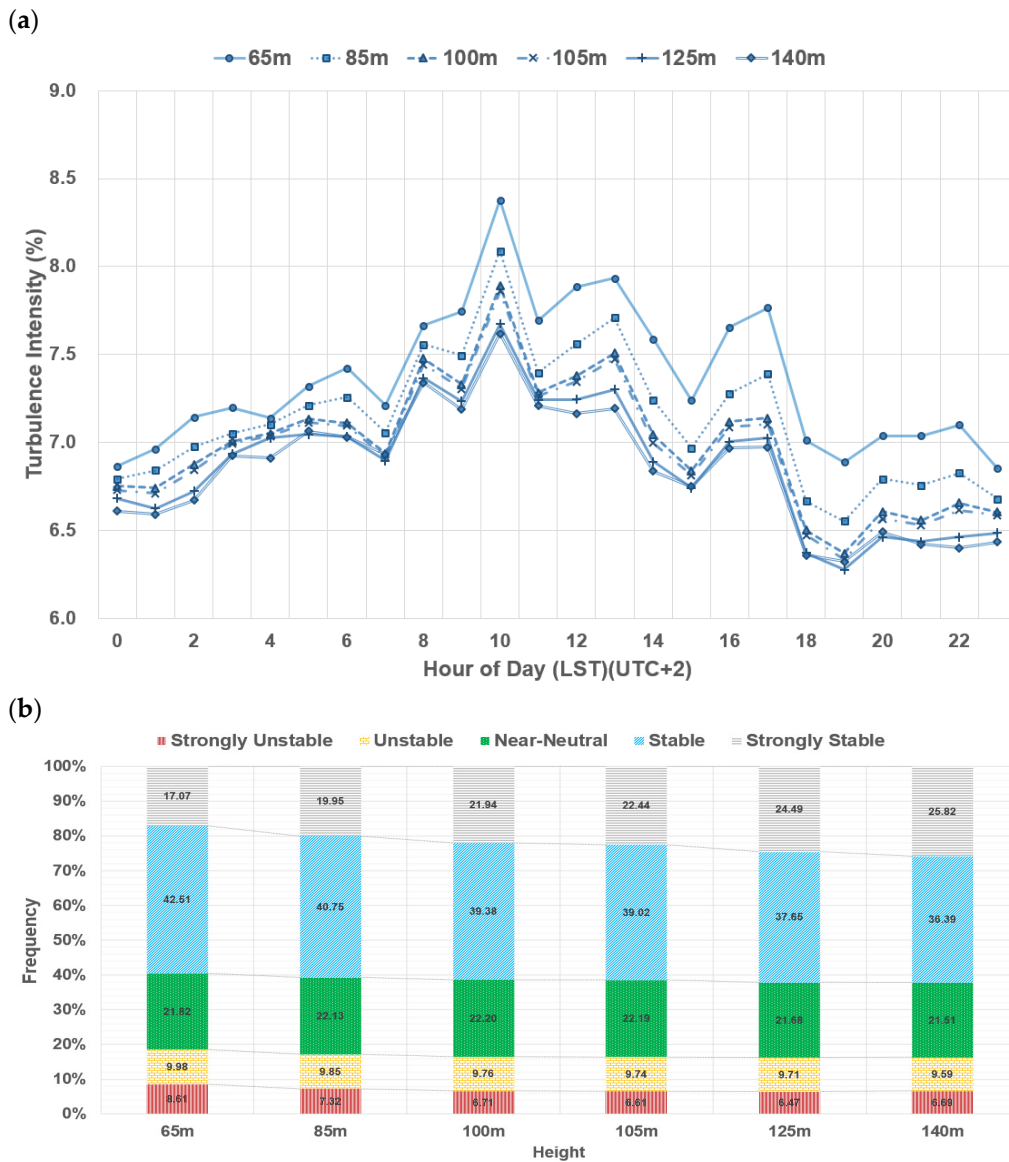
Figure 18. (**a**) Daily change in turbulence intensity, and (**b**) atmospheric stability frequency distribution ratio for each height. Turbulence intensity at hub height (85 m) has a peak time at 10 LST, value of 7.84%, and the atmospheric stability is stable.

Finally, the atmospheric stability is classified according to the Richardson number. The atmospheric stability analysis by wind shear and turbulence intensity described above corresponds to the mechanical atmospheric stability classification method that does not consider thermal factors. However, since the Richardson number uses temperature as a parameter, it is possible to define atmospheric stability according to temperature, and furthermore, heat flux distribution within the atmospheric boundary layer. Atmospheric stability based on the Richardson number was analyzed by dividing the upper part

(Sector #1) and lower part (Sector #2) of the rotor disk based on the hub height, and the entire rotor disk (Sector #3). According to the criteria for classification of atmospheric stability according to the Richardson number, the atmospheres in a strongly unstable and unstable state are indicated in red, neutral in green, and stable and strongly stable atmospheres in blue. Figure 19 shows the frequency of appearance of atmospheric stability by sector based on this standard.
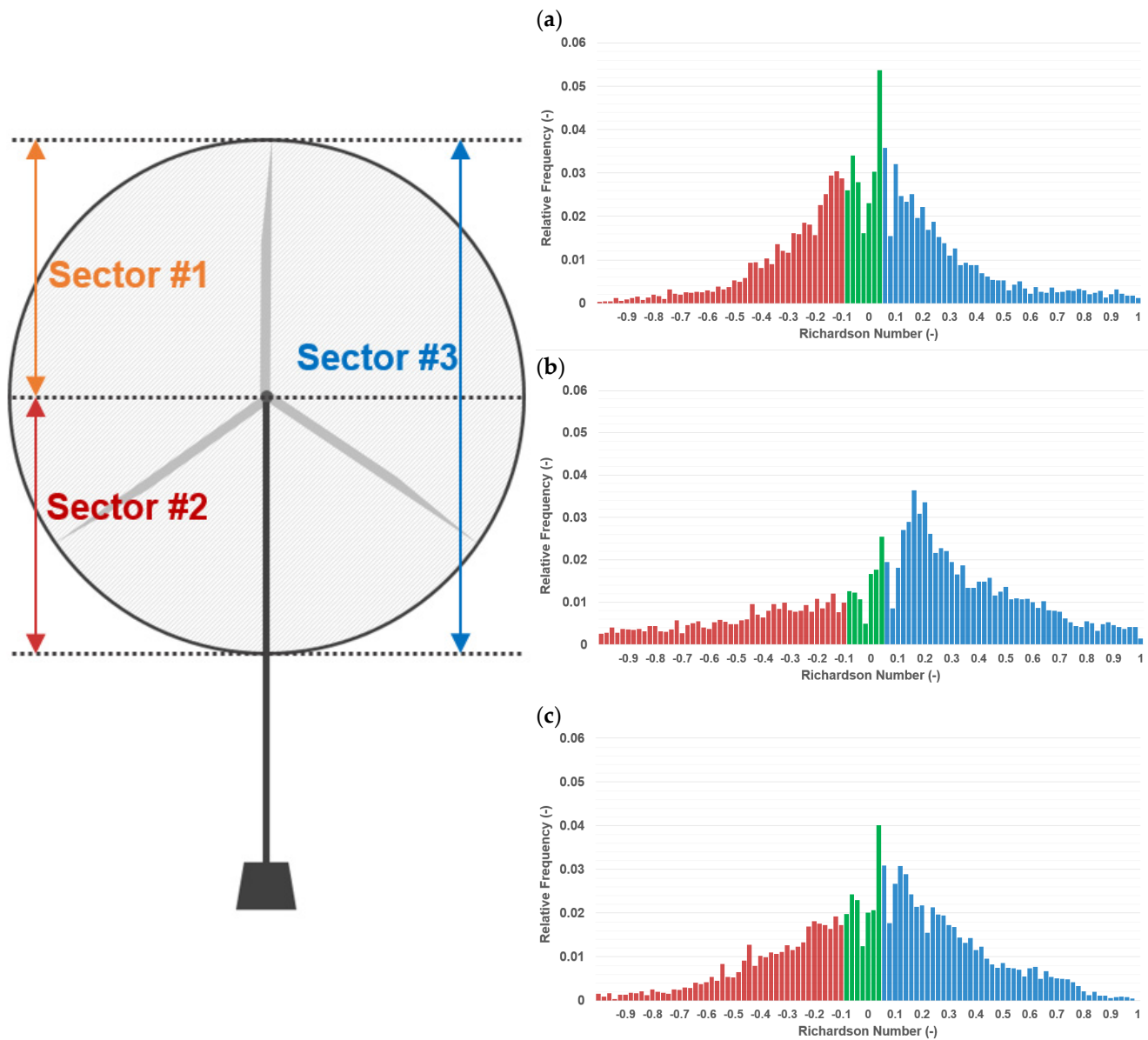

Figure 19. Sectors classified as upper, lower, and whole, based on the hub height for Richardson number analysis in the rotor disk area (**left**). On the right is the ratio of the frequency distribution of atmospheric stability by sector based on the Richardson number. Red indicates unstable (strongly unstable + unstable), green indicates near-neutral, and blue indicates stable atmosphere (stable + strongly stable). From (**a**–**c**), Sector #1, Sector #2, and Sector #3 are indicated, respectively.

It can be confirmed that above the rotor, the atmosphere in a stable or neutral state dominates, which does not receive radiation energy directly from the sea level. On the other hand, it was found that in the lower part of the rotor, relatively unstable atmospheric conditions frequently occurred. In the atmospheric stability based on the Richardson number calculated for the entire rotor disk, strong stable or unstable conditions were

dominant. On the other hand, the intraday change did not differ significantly from the average value. However, unlike the time-series on land, there was no significant change in atmospheric stability over time. In the case of the lower part of the rotor, the steady unstable state continued, and it can be confirmed that the relatively stable or neutral atmospheric state continues in the upper part of the rotor (Figure 20).
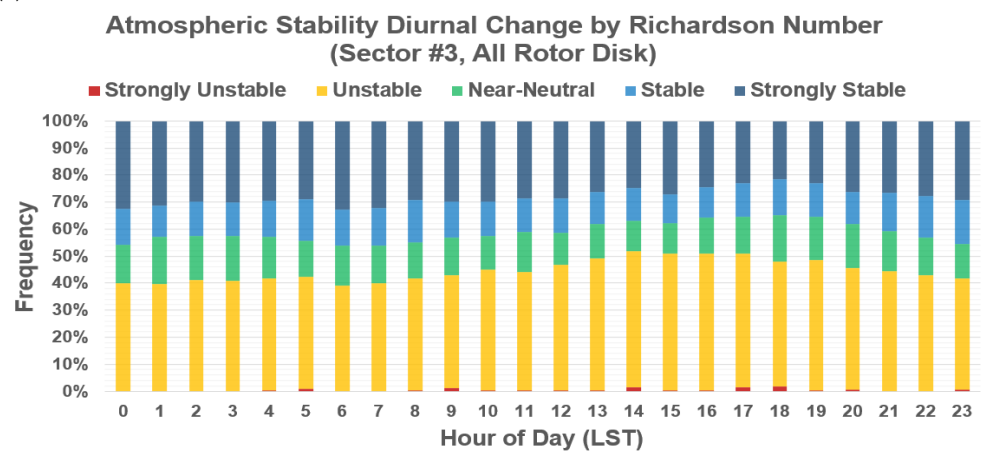
(**a**)
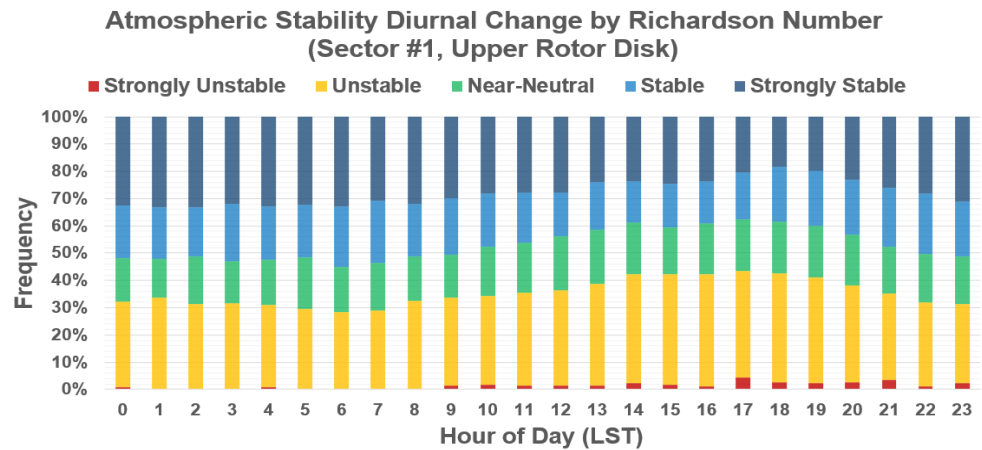
(**b**)
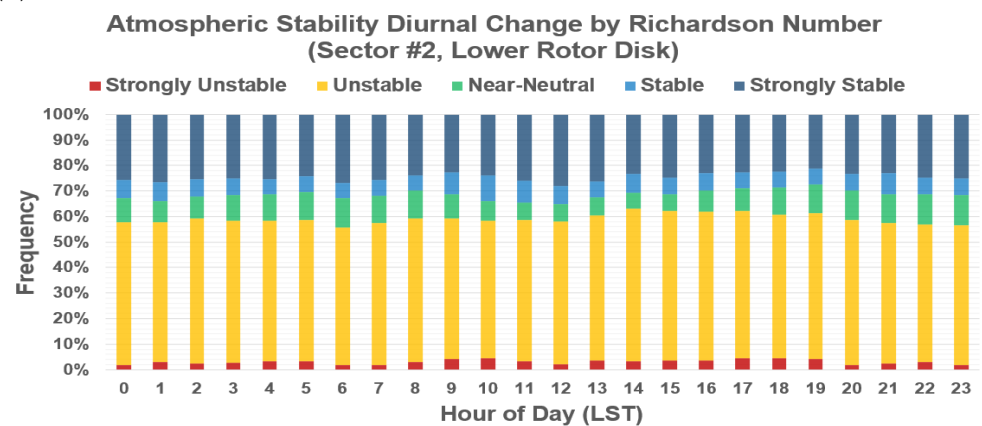
(**c**)

Figure 20. Daily change in Richardson Number through the wind turbine rotor disk area: (**a**) Sector #1, upper rotor disk area; (**b**) Sector #2, lower rotor disk area; and (**c**) Sector #3, whole rotor disk area.

3.5. Power Output Related with Atmospheric Stability

Based on the above atmospheric stability analysis results, we want to confirm the change in power generation according to atmospheric stability. In more detail, we examine how the error between the expected generation and actual generation based on REWS and HHWS changes, depending on atmospheric stability.

First, the wind shear-based wind power generation error rate for each atmospheric stability was calculated (Figure 21). When the atmosphere is unstable, neutral, or stable, HHWS sometimes has a smaller error rate, and there are turbines where REWS simulates the actual generation more closely. In particular, in the case of the A01 turbine with the widest free stream sector, it is the first turbine to receive wind from the upwind side, without the influence of wakes. Rather, in this case, it was shown that the simple HHWS simulates the actual power generation more closely than the REWS when the atmosphere is unstable, neutral, and stable. This is because when unstable, neutral, or stable, the vertical wind velocity profile is moderately inclined in the positive direction. On the other hand, when the atmosphere is strongly unstable or in a strong stable state, it can be seen that REWS significantly reduces the error with actual power generation compared to HHWS. In particular, when the atmosphere is strong and stable, the error rate with the actual power generation can be reduced by more than 5%.
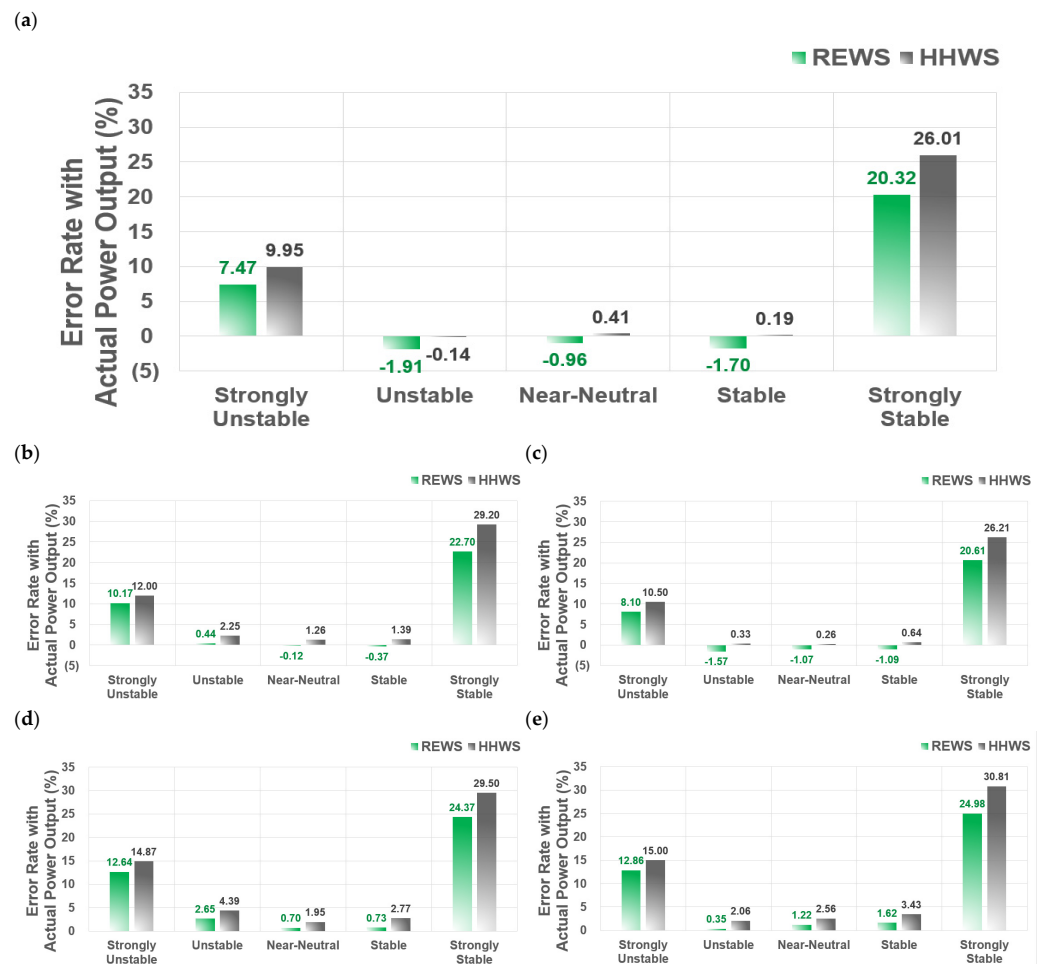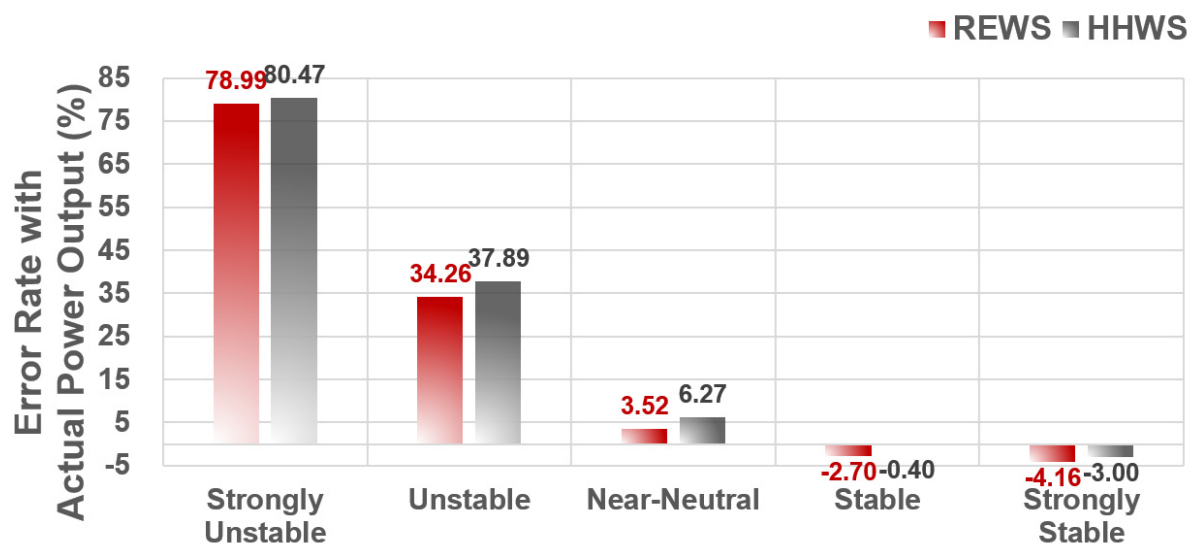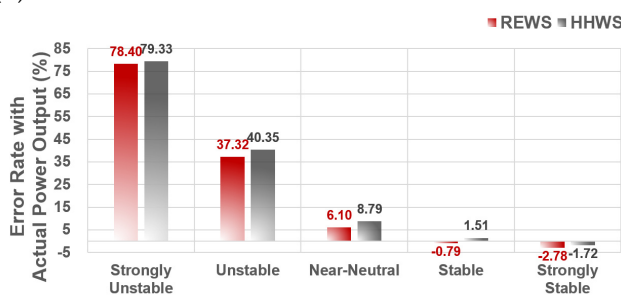

Figure 21. Comparison of error rate with actual power output by wind shear-based atmospheric stability classification. Green bar indicates the error rate between the REWS-based simulated power output and the actual power output, while gray indicates the error rate between the HHWS-based simulated and the actual power output. From (**a**–**e**), Turbine A01, Turbine A02, Turbine A03, Turbine B01 and Turbine C01 are indicated, respectively.

Second, the error rate of wind power generation by atmospheric stability was calculated based on the intensity of turbulence (Figure 22). This confirmed that when the atmosphere was strongly unstable or somewhat unstable, that is, when the turbulence intensity was high, both HHWS and REWS did not properly simulate the actual power generation. However, when the atmosphere was strongly unstable, unstable, or neutral, it could be confirmed that REWS improves the error rate with the actual power generation, compared to HHWS. On the other hand, when classifying atmospheric stability based on turbulence intensity, it was confirmed that when the atmosphere is strongly stable, that is, when turbulence hardly occurs, the simulated power generation based on HHWS is relatively closer to the actual power generation.
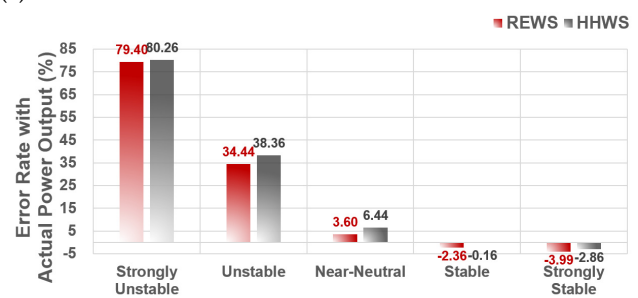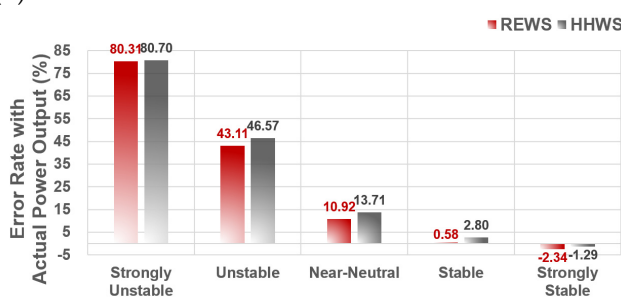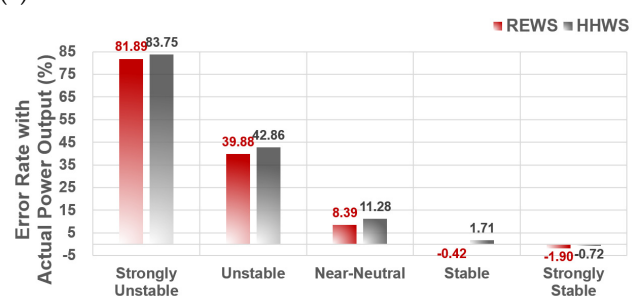

Figure 22. Comparison of error rate with actual power output by turbulence intensity-based atmospheric stability classification. Green bar indicates the error rate between the REWS-based simulated power output and the actual power output, while gray indicates the error rate between the HHWS-based simulated and the actual power output. From (**a**–**e**), Turbine A01, Turbine A02, Turbine A03, Turbine B01 and Turbine C01 are indicated, respectively.

Finally, the error rate of wind power generation by atmospheric stability was calculated based on the Richardson number (Figure 23). What is interesting here is that REWS only gives good results when the atmosphere is very unstable, i.e., within the atmospheric boundary layer, where free convection over mechanical convection dominates. Table 9 summarizes the error rates for each atmospheric stability index and the actual power generation.
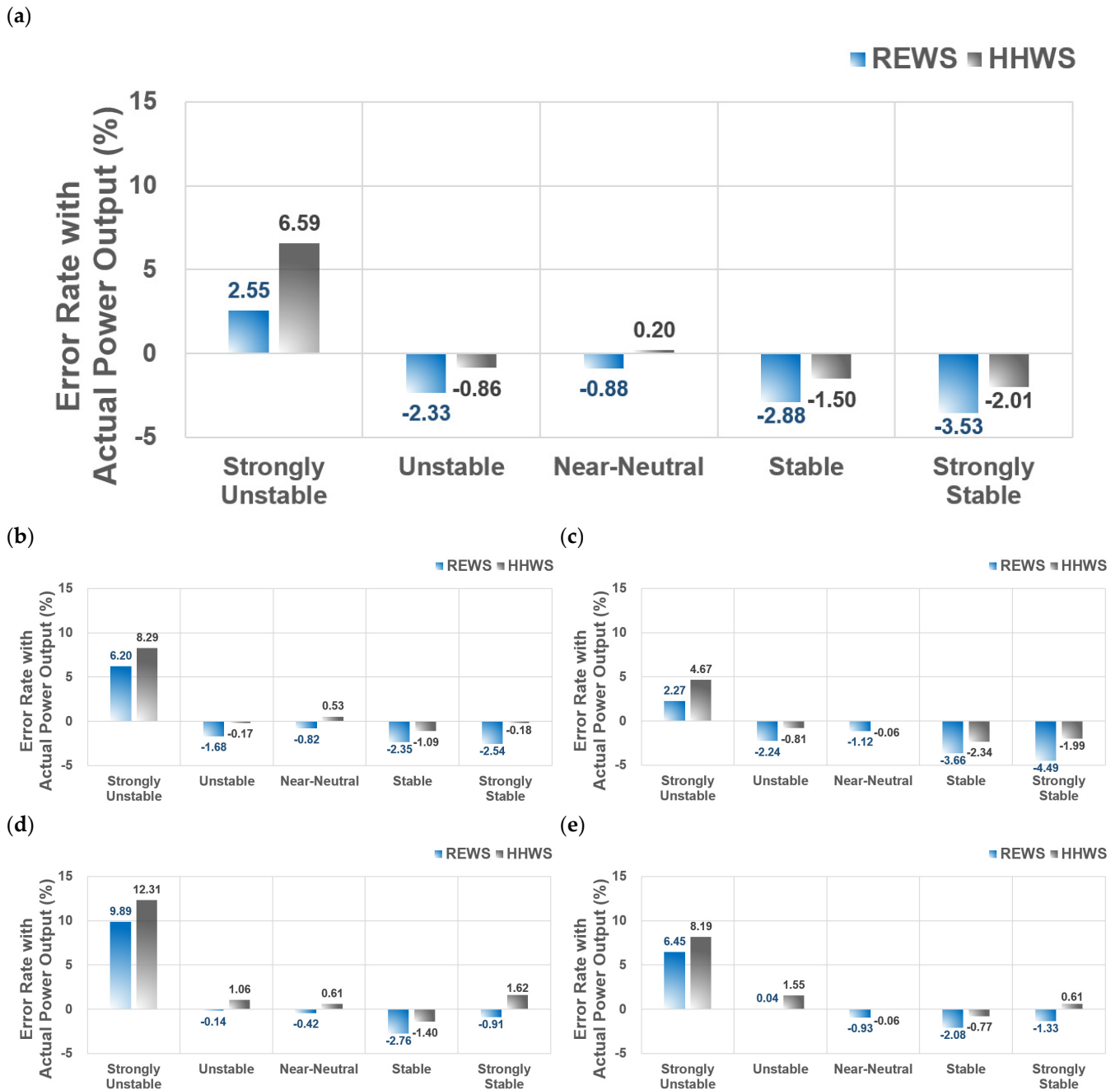
(**a**)

(**b**)　　　　　　　　　　　　　　　　　(**c**)

(**d**)　　　　　　　　　　　　　　　　　(**e**)

Figure 23. Comparison of error rate with actual power output by Richardson number-based atmospheric stability classification. Green bar indicates the error rate between the REWS-based simulated power output and the actual power output, while gray indicates the error rate between the HHWS-based simulated and the actual power output. From (**a**–**e**), Turbine A01, Turbine A02, Turbine A03, Turbine B01 and Turbine C01 are indicated, respectively.

Table 9. Error rate between the simulated power output based on REWS and HHWS, and the actual power output by atmospheric stability classification method (Wind shear, TI, Richardson Number).

Stability Index	Turbine No.	Compared with REWS (Error Rate, %)					Compared with HHWS (Error Rate, %)				
		1	2	3	4	5	1	2	3	4	5
Wind Shear	Turbine A01	7.47	−1.91	−0.96	−1.70	20.32	9.95	−0.14	0.41	0.19	26.01
	Turbine A02	10.17	0.44	−0.12	−0.37	22.70	12.00	2.25	1.26	1.39	29.20
	Turbine A03	8.10	−1.57	−1.07	−1.09	20.61	10.50	0.33	0.26	0.64	26.21
	Turbine B01	12.64	2.65	0.70	0.73	24.37	14.87	4.39	1.95	2.77	29.50
	Turbine C01	12.86	0.35	1.22	1.62	24.98	15.00	2.06	2.56	3.43	30.81
TI	Turbine A01	78.99	34.26	3.52	−2.70	−4.16	80.47	37.89	6.27	−0.40	−3.00
	Turbine A02	78.40	37.32	6.10	−0.79	−2.78	79.33	40.35	8.79	1.51	−1.72
	Turbine A03	79.40	34.44	3.60	−2.36	−3.99	80.26	38.36	6.44	−0.16	−2.86
	Turbine B01	80.31	43.11	10.92	0.58	−2.34	80.70	46.57	13.71	2.80	−1.29
	Turbine C01	81.89	39.88	8.39	−0.42	−1.90	83.75	42.86	11.28	1.71	−0.72
Richardson Number	Turbine A01	2.55	−2.33	−0.88	−2.88	−3.53	6.59	−0.86	0.20	−1.50	−2.01
	Turbine A02	6.20	−1.68	−0.82	−2.35	−2.54	8.29	−0.17	0.53	−1.09	−0.18
	Turbine A03	2.27	−2.24	−1.12	−3.66	−4.49	4.67	−0.81	−0.06	−2.34	−1.99
	Turbine B01	9.89	−0.14	−0.42	−2.76	−0.91	12.31	1.06	0.61	−1.40	1.62
	Turbine C01	6.45	0.04	−0.93	−2.08	−1.33	8.19	1.55	−0.06	−0.77	0.61

Atmospheric Stability Class (1: Strongly Unstable, 2: Unstable, 3: Near-Neutral, 4: Stable, 5: Strongly Stable).

4. Discussion

It is necessary to introduce some additional points to mention about this research method and some points to be supplemented in the future. First, WindSim, a commercial CFD software, was used in consideration of the fact that there was land on the upwind side and that there were more than 100 wind turbines and the turbines were closely spaced. Additionally, WRF, which has excellent predictability reflecting meteorological factors and is evaluated as the most commonly used numerical weather prediction model in the world, was judged to be suitable for this study. Second, most of the actual temperature data that can determine thermal atmospheric stability among the two-year offshore LiDAR observation data were missing. Fortunately, observation data for one month was secured, so it could be supplemented and verified with ERA5 reanalysis data, but actual observation data could further improve reliability. Third, along with the Richardson number, the Monin–Obukhov length, which is known as a representative method for determining thermal atmospheric stability, could not be calculated. It is a method to determine whether the turbulent momentum is due to the shear effect or the buoyancy effect through the mechanical variable of friction velocity, the natural variable of buoyancy, and the advection of heat flux. Since there was no flux sensor, the Monin–Obukhov length could not be calculated. There is a method of using reanalysis data, such as ERA5 or MERRA2, but it was not used because verification with actual data was not possible. Fourth, since it is an offshore wind farm, thermal stability is judged to have a strong correlation with sea surface temperature, as well as air temperature. In the future, by securing sea surface temperature data, it is intended to analyze the changes in REWS and HHWS according to the difference in sea surface temperature compared to the 20~30 average years.

5. Conclusions

In general, wind resources near the surface or sea level within the atmospheric boundary layer have very low predictability, because they induce characteristic changes in a short time by convection, temperature reversal layer, and wind shear caused by simultaneous forcing by mechanical and thermal factors. Accurately predicting wind power resources means accurately predicting wind power generation, which, in turn, can be a sure means of balancing electricity demand and supply with economic benefits for operators. In this study, in order to improve the prediction accuracy of wind power output, the concept of equivalent rotor wind speed recommended by IEC61400-12-1 was introduced to accurately reflect the wind speed characteristics of the rotor disk area. To determine how accurate and always accurate REWS compared to HHWS (Hub Altitude Wind Speed), two years of

SCADA data were analyzed and validated at the Anholt Offshore Wind Farm in Denmark. After filtering to secure valid data that satisfies the purpose of the study, 41.6% of the final data was analyzed. REWS- and HHWS-based simulated power output have different error rates than actual power output over each time. From midnight to 14:00, the error rate (−0.11%) between REWS-based simulated power output and actual power output tended to decrease compared to the error rate of HHWS (1.56%). The difference in accuracy of each method according to time change is directly related to the atmospheric stability. The cause of this difference can be explained by analyzing the gradient and shape of the vertical wind speed profile, how high the turbulence intensity is, and how the temperature or heat flux distribution differs from other regions. Wind shear, turbulence intensity, and Richardson number, which are the most commonly used atmospheric stability classification methods, were used because wind resource analysis based on local atmospheric stability is essential to increase the accuracy of power output prediction. In the vicinity of the Anholt offshore wind farm, unstable atmospheric conditions (59.13%) were dominant rather than stable (18.54%) in the wind shear-based atmospheric stability classification. This means that the wind speed difference between the upper and lower layers is small, and it also means that a lot of mixing effects are taking place in the vertical direction. As a result of the classification of atmospheric stability according to the turbulence intensity, a stable atmosphere was dominant (61.46%), and it is judged that this area does not generate much turbulence. In the results of atmospheric stability classification by Richardson number, the unstable atmosphere was dominant (42.71%), while the strongly stable atmosphere was also found in a significant proportion (39.07%). As a result of comparing the error rate between the actual and the simulated power output (REWS, HHWS) according to the atmospheric stability classification criteria, the error rate was large when the wind shear-based atmospheric stability classification was very stable (22.59%, 28.35%). This means that when the wind speed difference between the upper and lower layers is large and strong wind shear occurs in the vertical direction, the error rate is large. The error rates were large (10.25%, 12.46%) even when the atmosphere was very unstable. However, in both cases, the prediction accuracy of REWS-based simulation was improved. In the results of classification of atmospheric stability according to the turbulence intensity, the REWS showed that the error rate was low when the atmosphere was strongly unstable (79.79%) or unstable (37.80%), but the error rate was basically very large. Finally, as a result of analyzing the error rate for each atmospheric stability based on the Richardson number, the REWS consistently improved only when the atmosphere was strongly unstable (5.47%).

Through the results of this study, REWS, which is judged to be theoretically superior, showed better prediction accuracy than HHWS. However, this was not always the case, probably due to differences in atmospheric stability distribution based on local atmospheric boundary layer characteristics. In other words, when a wind farm project is to be carried out, it should be possible to determine which method, REWS or HHWS, can produce relatively more accurate power output based on the results of analysis of nearby atmospheric stability characteristics. Occasionally, the expected power output was small and the business license should be sold because it was thought that the project feasibility was insufficient, but the actual power output was higher. Conversely, the project was carried out because the expected power output was high, but the actual power output may be much lower. In order to reduce this severe risk, methodological research that can accurately calculate annual energy production should be continued. The author argues that in order to further expand and improve the technological maturity of wind energy, basic research on regional wind resources in the area where the project will be carried out should be completed in detail. The results of this study could be interpreted completely differently in other regions or countries. This is because latitude and longitude, air temperature, sea surface temperature, and amphibious distribution show very large differences from region to region. However, this study is expected to be widely used as basic data for developers and researchers who want a detailed analysis of offshore wind resources.

References

1. Sovacool, B.K.; Griffiths, S.; Kim, J.; Bazilian, M. Climate Change and Industrial F-Gases: A Critical and Systematic Review of Developments, Sociotechnical Systems and Policy Options for Reducing Synthetic Greenhouse Gas Emissions. *Renew. Sustain. Energy Rev.* **2021**, *141*, 110759. [CrossRef]
2. Nong, D.; Simshauser, P.; Nguyen, D.B. Greenhouse gas emissions vs CO_2 emissions: Comparative analysis of a global carbon tax. *Appl. Energy* **2021**, *298*, 117223. Available online: https://www.sciencedirect.com/science/article/pii/S0306261921006462 (accessed on 15 April 2022). [CrossRef]
3. O'Shaughnessy, E.; Heeter, J.; Shah, C.; Koebrich, S. Corporate Acceleration of the Renewable Energy Transition and Implications for Electric Grids. *Renew. Sustain. Energy Rev.* **2021**, *146*, 111160. [CrossRef]
4. Murshed, M. Can Regional Trade Integration Facilitate Renewable Energy Transition to Ensure Energy Sustainability in South Asia? *Energy Rep.* **2021**, *7*, 808–821. [CrossRef]
5. Meinshausen, M.; Lewis, J.; McGlade, C.; Gütschow, J.; Nicholls, Z.; Burdon, R.; Cozzi, L.; Hackmann, B. Realization of Paris Agreement Pledges May Limit Warming Just below 2 °C. *Nature* **2022**, *604*, 304–309. [CrossRef]
6. Hwangbo, S.; Heo, S.; Yoo, C. Development of Deterministic-Stochastic Model to Integrate Variable Renewable Energy-Driven Electricity and Large-Scale Utility Networks: Towards Decarbonization Petrochemical Industry. *Energy* **2022**, *238*, 122006. [CrossRef]
7. Chang, S.; Cho, J.; Heo, J.; Kang, J.; Kobashi, T. Energy Infrastructure Transitions with PV and EV Combined Systems Using Techno-Economic Analyses for Decarbonization in Cities. *Appl. Energy* **2022**, *319*, 119254. [CrossRef]
8. Park, J.; Kim, B. An Analysis of South Korea's Energy Transition Policy with Regards to Offshore Wind Power Development. *Renew. Sustain. Energy Rev.* **2019**, *109*, 71–84. [CrossRef]
9. Alataş, S.; Karakaya, E.; Hiçyılmaz, B. What Does Input Substitution Tell Us in Helping Decarbonization and Dematerialization? Industry Level Analysis for South Korea. *Sustain. Prod. Consum.* **2021**, *27*, 411–424. [CrossRef]
10. Jeong, W.-C.; Lee, D.-H.; Roh, J.H.; Park, J.-B. Scenario Analysis of the GHG Emissions in the Electricity Sector through 2030 in South Korea Considering Updated NDC. *Energies* **2022**, *15*, 3310. [CrossRef]
11. Tran, T.-T.; Kim, E.; Lee, D. Development of a 3-Legged Jacket Substructure for Installation in the Southwest Offshore Wind Farm in South Korea. *Ocean Eng.* **2022**, *246*, 110643. [CrossRef]
12. Ryu, G.H.; Kim, Y.-G.; Kwak, S.J.; Choi, M.S.; Jeong, M.-S.; Moon, C.-J. Atmospheric Stability Effects on Offshore and Coastal Wind Resource Characteristics in South Korea for Developing Offshore Wind Farms. *Energies* **2022**, *15*, 1305. [CrossRef]
13. Chu, K.H.; Lim, J.; Mang, J.S.; Hwang, M.-H. Evaluation of Strategic Directions for Supply and Demand of Green Hydrogen in South Korea. *Int. J. Hydrogen Energy* **2022**, *47*, 1409–1424. [CrossRef]
14. Chen, J.; Kim, M.-H. Review of Recent Offshore Wind Turbine Research and Optimization Methodologies in Their Design. *J. Mar. Sci. Eng.* **2022**, *10*, 28. [CrossRef]
15. Wang, L.; Kolios, A.; Liu, X.; Venetsanos, D.; Rui, C. Reliability of Offshore Wind Turbine Support Structures: A State-of-the-Art Review. *Renew. Sustain. Energy Rev.* **2022**, *161*, 112250. [CrossRef]
16. Pryor, S.C.; Barthelmie, R.J.; Shepherd, T.J. Wind Power Production from Very Large Offshore Wind Farms. *Joule* **2021**, *5*, 2663–2686. [CrossRef]
17. Ren, Z.; Verma, A.S.; Li, Y.; Teuwen, J.J.E.; Jiang, Z. Offshore wind turbine operations and maintenance: A state-of-the-art review. *Renew. Sustain. Energy Rev.* **2021**, *144*, 110886. [CrossRef]
18. Offshore Wind Turbines: Size Really Matters, Rystad Says. Offshore Engineer Magazine. 2020. Available online: https://www.oedigital.com/news/481796-offshore-wind-turbines-size-really-matters-rystad-says (accessed on 3 May 2022).
19. Zhu, J.; Cai, X.; Ma, D.; Zhang, J.; Ni, X. Improved Structural Design of Wind Turbine Blade Based on Topology and Size Optimization. *Int. J. Low-Carbon Technol.* **2022**, *17*, 69–79. [CrossRef]

20. Bilgili, M.; Tumse, S.; Tontu, M.; Sahin, B. Effect of Growth in Turbine Size on Rotor Aerodynamic Performance of Modern Commercial Large-Scale Wind Turbines. *Arab. J. Sci. Eng.* **2021**, *46*, 7185–7195. [CrossRef]

21. Ryu, G.-H.; Kim, D.-H.; Lee, H.-W.; Park, S.-Y.; Yoo, J.-W.; Kim, H.-G. Accounting for the Atmospheric Stability in Wind Resource Variations and Its Impacts on the Power Generation by Concentric Equivalent Wind Speed. *J. Korean Sol. Energy Soc.* **2016**, *36*, 49–61. [CrossRef]

22. Ryu, G.-H.; Kim, D.-H.; Lee, H.-W.; Park, S.-Y.; Kim, H.-G. A Study of Energy Production Change according to Atmospheric Stability and Equivalent Wind Speed in the Offshore Wind Farm using CFD Program. *J. Environ. Sci. Int.* **2016**, *25*, 247–257. [CrossRef]

23. Scheurich, F.; Enevoldsen, P.B.; Paulsen, H.N.; Dickow, K.K.; Fiedel, M.; Loeven, A.; Antoniou, I. Improving the Accuracy of Wind Turbine Power Curve Validation by the Rotor Equivalent Wind Speed Concept. *J. Phys. Conf. Ser.* **2016**, *753*, 072029. [CrossRef]

24. Van Sark, W.; Van der Velde, H.C.; Coelingh, J.P.; Bierbooms, W. Do we really need rotor equivalent wind speed? *Wind Energy* **2019**, *22*, 745–763. [CrossRef]

25. Jeon, S.; Kim, B.; Huh, J. Study on methods to determine rotor equivalent wind speed to increase prediction accuracy of wind turbine performance under wake condition. *Energy Sustain. Dev.* **2017**, *40*, 41–49. [CrossRef]

26. Wagner, R.; Antoniou, I.; Pedersen, S.M.; Courtney, M.S.; Jørgensen, H.E. The influence of the wind speed profile on wind turbine performance measurements. *Wind Energy* **2009**, *12*, 348–362. [CrossRef]

27. *IEC 61400-12-1*; Wind Turbines-Part 12-1: Power Performance Measurements of Electricity Producing Wind Turbines. International Electrotechnical Commission: Geneva, Switzerland, 2005.

28. Wharton, S.; Lundquist, J. Atmospheric stability effects wind turbine power collection. *Environ. Res. Lett.* **2012**, *7*, 014005. [CrossRef]

29. DuPont, B.L.; Cagan, J.; Moriarty, P. Optimization of Wind Farm Layout and Wind Turbine Geometry Using a Multi-Level Extended Pattern Search Algorithm That Accounts for Variation in Wind Shear Profile Shape. In Proceedings of the ASME 2012 International Design Engineering Technical Conferences and Computers and Information in Engineering Conference, Chicago, IL, USA, 12–15 August 2012; American Society of Mechanical Engineers Digital Collection: New York, NY, USA, 2013; pp. 243–252. [CrossRef]

30. Redfern, S.; Olson, J.B.; Lundquist, J.K.; Clack, C.T.M. Incorporation of the Rotor-Equivalent Wind Speed into the Weather Research and Forecasting Model's Wind Farm Parameterization. *Mon. Weather Rev.* **2019**, *147*, 1029–1046. [CrossRef]

31. Sasser, C.; Yu, M.; Delgado, R. Improvement of Wind Power Prediction from Meteorological Characterization with Machine Learning Models. *Renew. Energy* **2022**, *183*, 491–501. [CrossRef]

32. Choukulkar, A.; Pichugina, Y.; Clack, C.T.M.; Calhoun, R.; Banta, R.; Brewer, A.; Hardesty, M. A New Formulation for Rotor Equivalent Wind Speed for Wind Resource Assessment and Wind Power Forecasting. *Wind Energy* **2016**, *19*, 1439–1452. [CrossRef]

33. Bardal, L.M.; Sætran, L.R.; Wangsness, E. Performance Test of a 3MW Wind Turbine—Effects of Shear and Turbulence. *Energy Procedia* **2015**, *80*, 83–91. [CrossRef]

34. Murphy, P.; Lundquist, J.K.; Fleming, P. How wind speed shear and directional veer affect the power production of a megawatt-scale operational wind turbine. *Wind Energy Sci.* **2020**, *5*, 1169–1190. [CrossRef]

35. Zhan, L.; Letizia, S.; Valerio Iungo, G. LiDAR Measurements for an Onshore Wind Farm: Wake Variability for Different Incoming Wind Speeds and Atmospheric Stability Regimes. *Wind Energy* **2020**, *23*, 501–527. [CrossRef]

36. Radünz, W.C.; Sakagami, Y.; Haas, R.; Petry, A.P.; Passos, J.C.; Miqueletti, M.; Dias, E. Influence of Atmospheric Stability on Wind Farm Performance in Complex Terrain. *Appl. Energy* **2021**, *282*, 116149. [CrossRef]

37. Wise, A.S.; Neher, J.M.T.; Arthur, R.S.; Mirocha, J.D.; Lundquist, J.K.; Chow, F.K. Meso- to Microscale Modeling of Atmospheric Stability Effects on Wind Turbine Wake Behavior in Complex Terrain. *Wind Energy Sci.* **2022**, *7*, 367–386. [CrossRef]

38. Han, X.; Liu, D.; Xu, C.; Shen, W.Z. Atmospheric Stability and Topography Effects on Wind Turbine Performance and Wake Properties in Complex Terrain. *Renew. Energy* **2018**, *126*, 640–651. [CrossRef]

39. Kim, D.-Y.; Kim, Y.-H.; Kim, B.-S. Changes in Wind Turbine Power Characteristics and Annual Energy Production Due to Atmospheric Stability, Turbulence Intensity, and Wind Shear. *Energy* **2021**, *214*, 119051. [CrossRef]

40. Guo, N.; Zhang, M.; Li, B.; Cheng, Y. Influence of Atmospheric Stability on Wind Farm Layout Optimization Based on an Improved Gaussian Wake Model. *J. Wind Eng. Ind. Aerodyn.* **2021**, *211*, 104548. [CrossRef]

41. St. Martin, C.M.; Lundquist, J.K.; Clifton, A.; Poulos, G.S.; Schreck, S.J. Wind Turbine Power Production and Annual Energy Production Depend on Atmospheric Stability and Turbulence. *Wind Energy Sci.* **2016**, *1*, 221–236. [CrossRef]

42. Peña, A.; Schaldemose Hansen, K.; Ott, S.; van der Laan, M.P. On Wake Modeling, Wind-Farm Gradients, and AEP Predictions at the Anholt Wind Farm. *Wind Energy Sci.* **2018**, *3*, 191–202. [CrossRef]

43. Archer, C.L.; Vasel-Be-Hagh, A.; Yan, C.; Wu, S.; Pan, Y.; Brodie, J.F.; Maguire, A.E. Review and Evaluation of Wake Loss Models for Wind Energy Applications. *Appl. Energy* **2018**, *226*, 1187–1207. [CrossRef]